Journal of Materials Chemistry A

PAPER

Check for updates

Cite this: J. Mater. Chem. A, 2019, 7, 10781

Phase transformations and capacity fade mechanism in Li_xSn nanoparticle electrodes revealed by operando ^{7}Li NMR†

Jose L. Lorie Lopez, Philip J. Grandinetti * and Anne C. Co *

Operando ^{7}Li nuclear magnetic resonance (NMR), *ex situ* ^{7}Li magic-angle spinning (MAS) NMR and pair distribution function (PDF) methods are used to investigate the electrochemical lithiation and delithiation of 60 nm particles of tin. While the structural transformation pathways between Li–Sn intermetallics during lithiation and delithiation of Sn nanoparticles are somewhat consistent with the structural evolution of Li–Sn phases expected from the equilibrium binary phase diagram, there are some notable exceptions with the observation of a metastable phase Li_2Sn_3, and two vacancy rich metastable phases, $Li_{7-\zeta}Sn_3$, and $Li_{13-\delta}Sn_5$ during delithiation. The capacity fade of ~30% per cycle is not attributed to particle cracking, but rather to particles losing contact with the carbon/PVDF binder. The disconnecting particles are associated with Li_xSn phases undergoing large decreases in diameters on delithiation, *i.e.*, Sn, Li_2Sn_5, LiSn, and Li_7Sn_3. A peculiar behavior of capacity fade in this system is that it only occurs during delithiation. This is explained by a model of disconnecting–reconnecting Li_xSn-containing particles which remain in the electrode and become reconnected every cycle by the volume increase of neighboring connected particles during the lithiation process.

Received 26th February 2019
Accepted 1st April 2019

DOI: 10.1039/c9ta03345a

rsc.li/materials-a

1 Introduction

The demand for inherently safe, large capacity, portable energy storage has led to the investigation of a class of anode materials that form stable intermetallic compounds with lithium,[1–5] such as Si, Sn, Sb, Ge, As, Al, providing Li storage capacities 3 to 10 times that of graphite. Of the various intermetallic anodes, tin has received significant attention due to its high theoretical gravimetric and volumetric capacities,[6] 960 mA h g^{-1} and 6971 mA h cm^{-3} respectively, its low potential 0.5 V *vs.* Li/Li^+,[7] and more importantly, its high electrical conductivity of about 8.7×10^4 S cm^{-1}.

Despite their high capacity, intermetallics have not lived up to expectations for portable energy storage due to significant capacity fade over each cycle.[8] Considerable progress has been made in the last two decades in understanding the macro- and microscopic mechanisms behind this capacity fade—providing inspiration for the design of new classes of nano-structured electrodes. Nonetheless, these efforts continue to remain hindered by fundamental gaps in our understanding of the structural transformation pathways during electrochemical lithiation and delithiation, their thermodynamics and kinetics, and role in mechanisms of capacity fade.

The electrochemical lithiation transformation path suggested by the equilibrium binary phase diagram[9,10] of lithium and tin proceeds through the sequential formation of intermetallic phases, Li_2Sn_5, LiSn, Li_7Sn_3, Li_5Sn_2, $Li_{13}Sn_5$, Li_7Sn_2, and $Li_{22}Sn_5$, with increasing lithium content. Rhodes *et al.*,[11] however, performed *in situ* X-ray measurements on 5 μm thin film Sn electrodes and detected only β-Sn, Li_2Sn_5, LiSn, and $Li_{22}Sn_5$. This result was consistent with earlier *in situ* X-ray measurements by Courtney and Dahn[6] on a variety of tin oxide based compounds, where the oxides were reduced to Sn upon lithiation. These results suggested that the lithium-rich phases could not form long-range ordered structures due to the low mobility at room temperature and the large volume changes.

A major factor in the capacity fade in all intermetallics is the large volume expansions upon lithiation—up to 300% of their initial structure—which leads to pulverization and amorphization of the electrode and disconnected particles.[8,12–18] While one might suspect that amorphization might also be a cause of remaining capacity fade, it is not likely as amorphous Si- and Sn-based anodes have been reported to significantly improve the reversibility compared to their crystalline counterpart.[14] For example, Beaulieu *et al.*[13] reported reversible volume expansion of amorphous Si and Sn alloys prepared from magnetron sputtering and later concluded that the eventual capacity fade is due to loss in electrode contact. Hatchard *et al.*[14] also showed that a dramatic

Department of Chemistry, The Ohio State University, 100 West 18th Ave., Columbus, OH, 43210-1340, USA. E-mail: grandinetti.1@osu.edu; co.5@osu.edu

† Electronic supplementary information (ESI) available: Additional details on sample characterization: variable temperature *in situ* and *ex situ* MAS NMR spectra, SEM, surface profilometry, and XPS. We also provide the .cif file of the $Li_{7-\zeta}Sn_3$ supercell obtained from the PDF analysis. See DOI: 10.1039/c9ta03345a

fade in capacity is observed when crystalline phases are present in a predominantly amorphous $Si_{1-x-y}Al_xSn_y$ alloy.

Yang *et al.*[12] found that reducing the active Sn particle size from 3 μm to 300 nm improves the cycle stability of alloy anodes. This improved stability with reducing particle sizes to the nanometer range (<100 nm) is now well documented in other systems[8,19] and is primarily attributed to the ability of nanosized particles to accommodate large stress and strain of volume changes during lithiation and delithiation without cracking.

Even with nanosize Sn particles, however, capacity fade remains significant, particularly when cycled to more reductive potentials down to 0.2 V. It is well established that the formation of an solid electrolyte interface (SEI) surface film[20,21] on alloy particles causes capacity fade. This interface consists mainly of Li_2CO_3, various lithium alkylcarbonates ($ROCO_2Li$), LiF, Li_2O and nonconductive polymers. Another well known cause of irreversible loss of lithium is the decomposition reaction of (surface) oxides present on a metallic film or particle. This occurs primarily in the first cycle as native oxides present, usually in the form of passivation surface oxides or in bulk tin oxides, are reduced to amorphous Li_2O. After the first few cycles the loss of lithium from oxide decomposition and SEI formation is diminished, particularly when cracking of the active material can be avoided through nano-sizing.

The origin of the continuing capacity fade after the first few cycles is less understood. The electrochemical aggregation of nano-sized alloy particles[5,6] has also been identified as a possible mechanism causing capacity fade. The aggregation of active particles over many cycles[6] is thought to cause irreversible capacity loss from increased Li diffusion lengths and the trapping of SEI films inside aggregated particles.[22] To avoid this aggregation efforts have focused on dispersing active alloy particles within a suitable host matrix to buffer the large volume change and act as a spacer during cycling.[8] Another hypothesis for explaining the additional capacity fade is the irreversible trapping by host atoms. This was suggested by Li *et al.*[22,23] for nano sized Si and SnSb alloy anodes where it was thought that Li became irreversible bound to low coordinated Si or Sb defect sites on the surface and in the bulk.

Operando nuclear magnetic resonance is a powerful technique for probing structure and dynamics in battery materials.[24–26] Recently, we reported a signal processing approach called derivative Operando (dOp) NMR,[27] which simply involves taking the derivative of the signal with respect to the operando time to improve the resolution of operando NMR spectra by removing time independent signals and to further distinguish between time dependent signals associated with the formation and removal of species.

Here, in an effort to understand better the thermodynamics and kinetics of electrochemical lithiation and delithiation of Sn as well as mechanisms of capacity fade, we employ operando ^{7}Li nuclear magnetic resonance (NMR), *ex situ* ^{7}Li magic-angle spinning (MAS) NMR and pair distribution function (PDF) methods to investigate 60 nm particles of tin—where the primary capacity fade from volume expansion and cracking is known to be eliminated.[8,12,19] We employ thermodynamically controlled cyclic voltammetry (CV) experiments (2.5 μV s^{-1}) to maintain a quasi-equilibrium throughout the lithiation and delithiation processes. This provides a clearer separation of thermodynamic and kinetic factors. It also is advantageous for enhancing resolution in the operando time dimension of the two-dimensional dOp NMR spectrum.

2 Materials and methods

2.1 Sample preparation

2.1.1 Sn electrode preparation. A slurry was prepared from 85 wt% (17 vol%) Sn nanopowder (60–80 nm, 99.99% metal basis, US Research Nanomaterials, Inc.) with 5 wt% (75 vol%) carbon black (Carbon Vulcan Black XC-72R) and 10 wt% (8 vol%) polyvinylidene fluoride (PVDF, MTI Corp.) in *N*-methylpyrrolidone (NMP, MTI Corp.). The slurry was casted on a thin copper foil (9 μm thick, MTI Corp.) current collector using an adjustable doctor blade (MSK-AFA I, MTI Corp.) set at a thickness of 0.4 mm followed by drying from 65 to 90 °C for 4 hours with intermittent vacuum. The electrodes were cut, weighed, and pressed to 5000 lbf using 2 stainless steel blocks of 6.75 cm × 10.25 cm surface area and a Carver 3851-00 Hydraulic Press. Each dry electrode contained about 3 mg of active material.

2.1.2 Electrochemical cell. A modified version of the bag cell battery configuration developed by Bellcore,[28] similar to that used by Letellier *et al.*,[29] was used in this study and is illustrated in Fig. 1. The two-electrode battery half-cells were assembled in an Ar filled glove box (mBraun) with continuous detection of H_2O (<0.5 ppm) and O_2 (<0.5 ppm). The Sn nanoparticle electrode served as the working electrode and a high purity lithium metal foil (0.3 mm thick, Chemetall Foote Corp.) served as combined counter and reference electrode. A 1 M solution of lithium hexafluorophosphate ($LiPF_6$) in a 1 : 1 v/v of ethyl carbonate (EC) and dimethyl carbonate (DMC) was used as the electrolyte (Purolyte A5 Series, Novolyte Technologies). The Sn and Li electrodes were separated by a Celgard® 2400 separator soaked in the electrolyte prior to assembly. The lithium electrode was pressed onto a copper mesh current collector and the stack was then enclosed and vacuum sealed in a polyethylene plastic bag inside the glove box. The electrochemical cell was 4 mm wide and 10 mm long and contained 2.8 mg of Sn.

2.2 Electrochemical measurements

A CHI400B (CH Instruments, Inc., Austin, TX) galvanostat/potentiostat was used to perform all electrochemical measurements in this work. All voltages were measured and reported

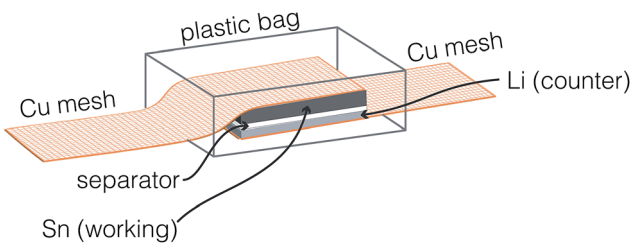

Fig. 1 Schematic of the bag cell used in the NMR measurements.

against Li/Li^+. The initial open circuit potential (OCP) of the cell was around 2.88 V. Two "fast" cyclic voltammograms (CV) between 1.0 and 0.2 V at a potential sweep of 1 mV s^{-1} were collected before placing the cell in the NMR probe to verify that the cell was cycling and the anticipated voltammogram of Sn was obtained. The electrochemical cell was then inserted in the NMR coil and connected to the potentiostat. Another 1 mV s^{-1} CV was measured between 1.0 and 0.2 V after which CVs were collected at 2.5 μV s^{-1} from 1.0 to 0.2 V and back to 1.0 V.

2.3 X-ray measurements

PDF studies were conducted at sector 11-ID-B of the Advanced Photon Source (APS) at Argonne National Laboratory. X-ray scattering measurements were performed at an operating energy of 86.72 keV ($\lambda = 0.1432$ Å). Tin electrodes were cycled at 2.5 μV s^{-1} to form the standard Li_7Sn_3 at 0.38 V (lithiation) and to $Li_{7-\zeta}Sn_3$ at 0.58 V (delithiation). The phases were confirmed by NMR prior to PDF measurements. Experimental geometries were calibrated using CeO_2 powder and FIT2D software.[30] FIT2D was also used to transform the data into a function of Q, and corrections for background, Compton scattering, and detector effects were applied. A Fourier transform was applied to obtain $G(r)$ using PDFGetX2 software.[31] PDFGui[32] was used to perform structural refinements.

2.4 NMR measurements

All NMR measurements were performed on a Bruker Avance III HD 400 MHz spectrometer. The ^{7}Li frequency shifts were referenced to a 1 M aqueous solution of lithium chloride (LiCl).

2.4.1 Operando study. The ^{7}Li operando NMR spectra in Fig. 3 and 6A were acquired at ambient temperature using a Bloch decay sequence with a Bruker static wideline probe and a 12 mm transceiver coil. The electrochemical bag cell was placed inside a cylindrical Vespel housing. The thickness of the battery was matched to the opening of the housing and Teflon shims were added above and below the cell to keep a uniform pressure applied across the cell and to maintain electrical contact. The housing was oriented with the electrode face parallel to B_0 in order to minimize magnetic susceptibility broadenings.[33] At the ^{7}Li NMR frequency (155.48 MHz) the skin depth in Sn metal is ~13 μm, and the thickness of the electrode is ~30 μm. With carbon particles occupying 75% of the volume in the Sn electrode, the 60 nm Sn particles are sufficiently separated that there are no significant rf skin depth effects affecting the quantification of ^{7}Li NMR signal intensities from the Sn electrode.

The NMR probe was modified to feed the wires connecting the potentiostat through the base of the probe to maintain a common ground with the probe circuit. Low pass filters were connected in line of the potentiostat cables to block high frequency noise injected from the potentiostat and eliminate stray rf picked up by the potentiostat cables from reaching the NMR receiver coil. The radio frequency transmitter power level was reduced to 50 watts to eliminate arcing in the coil, and corresponds to a rf field strength of $\omega_1/(2\pi) = 10$ kHz. At this power, only the central transitions of the Li metal nuclei are excited ($\omega_q \gg \omega_1$), as their magnetization nutates at twice the rate of lithium nuclei in the electrolyte and the Li_xSn compounds. Thus, at this power a 12.5 μs pulse length corresponds to 45° rotation of magnetization associated with all Li NMR transitions in the electrolyte and the Li_xSn compounds and a 90° rotation of magnetization associated only with the Li central NMR transitions in Li metal.

For operando NMR/cyclic voltammetry experiments the total acquisition time was 7.68 ms; a 2.5 s recovery time was used between scans; and 360 scans were averaged together for each spectrum. With these acquisition parameters each spectrum was obtained in 15 min giving an electrochemical resolution of 2.25 mV per NMR spectra. A total of 1474 spectra were acquired for a total measurement time of 368.25 h (approx. 15 days). Variations in the probe tuning while the potentiostat varied the voltage and current caused the initial phase of the NMR signal to vary over the full duration of the operando experiment. Thus, the time origin of all 1474 free induction decays were autophased to place maximum intensity in the real channel, and the 1474 1D spectra were then further phased as a single 2D signal. All spectral processing were performed with the program RMN.[34] The operando 2D ^{7}Li NMR spectrum shown in Fig. 3 was acquired during the 4th and 5th cycles of a Sn cell at 2.5 μV s^{-1}. The corresponding potentials at which lithiation and delithiation occur are shown on the right axis of Fig. 3.

The corresponding dOp NMR spectrum is shown in Fig. 3B. Positive derivative intensities are shown in green and represent formation of lithium species (henceforth called *formation resonance*) whereas negative derivative intensities are shown in red and represent the removal of lithium species (henceforth called *removal resonance*).

In situ ^{7}Li longitudinal relaxation times for Li sites were measured by the inversion recovery[35] method at ambient temperature in a separate but identical battery in a series of potential hold experiments to electrochemically synthesize the different Li_xSn phases. The approximate ^{7}Li longitudinal relaxation times are given in Table S1 (ESI†). The frequency assignments were based on the shifts of the Li–Sn intermetallic phases reported by Bekaert *et al.*[36]

In situ variable temperature spectra in Fig. S1A (ESI†) were performed using an rf power of 150 W. A 5 μs pulse length was used giving a tip angle of 36° for the intermetallics and electrolyte, and 72° for the Li metal. A recycle delay of 0.65 s was used and 440 scans were averaged together for each spectrum.

2.4.2 *Ex situ* MAS studies. For *ex situ* NMR MAS measurements, six different cells were cycled to the desired potentials at 2.5 μV s^{-1}, disassembled, and the material scraped from the current collector and mixed with polypropylene microbeads at a ratio of 1 : 1 (by weight) to reduce eddy currents and sample heating from the sample rotation, and improve radio frequency penetration in the metallic sample. Previously, MAS measurements were performed by mixing the lithiated materials with SiO_2 as the insulator,[36] however, the samples were unstable with loss of Li from the Li_xSn phases and an increase in the SEI NMR signal, likely due to the reaction of the SiO_2 with the Li in the intermetallic phases. The ^{7}Li *ex situ* MAS NMR spectra in Fig. 4 were acquired with a Bruker 2.5 mm MAS probe at a spinning speed of 20 kHz using a 15 s recycle delay, a π/2 pulse length of

a 4 μs at 50 W, and 64 scans. The ^{7}Li *ex situ* MAS NMR spectra in Fig. 6B were acquired with a Bruker 4 mm MAS probe using a 30 s recycle delay, and an rf π/2 pulse length of a 4 μs at 50 W, and 8 scans. The variable temperature ^{7}Li *ex situ* MAS NMR spectra in Fig. S1B (ESI†) were acquired with a Bruker 4 mm MAS probe at a spinning speed of 12 kHz and a π/2 pulse length of a 4 μs at 50 W, with 8 scans. A 45 s recycle delay was used for measurements between 243 K and 283 K, a 30 s recycle delay for measurements between 293 K and 333 K, and a 20 s delay for the measurements at 343 K and 353 K.

3 Results and discussion

A typical cyclic voltammogram (CV) of the fourth cycle of the 60 nm Sn electrode measured at 2.5 μV s^{-1} is shown in Fig. 2. For these experiments it was decided to run thermodynamically controlled experiments at sweep rates of 2.5 μV s^{-1} (~C/89), even though these are not practical for everyday battery use, in an attempt to keep the battery at a quasi-equilibrium throughout the process. While the polarization direction is reversed when the cell potential reaches 0.2 V, the return sweep in Fig. 2A remains reductive from 0.2 V to 0.32 V. Oxidative delithiation is observed at potentials higher than 0.32 V.

Five distinct reduction peaks (regions), labeled I, II, III, IV and V, are apparent during lithiation, and four oxidation peaks (regions), labeled I′, III′, IV′ and V′, are apparent during delithiation of Sn. From the onset potentials obtained from the CV, the specific capacities associated with each peak (region) were quantified and are given in Table 1. Fig. 2B shows the cell's specific capacity as a function of cell potential.

In the region from 1.0 to 0.72 V, that is, prior to peak I, a slow increase of lithium is transferred to the system. This capacity equivalent of 40.4 mA h g^{-1} (see Table 1) is likely due to SEI formation. Although this is the fourth cycle of the cell, small amounts of SEI are expected to continue forming on all Li_xSn phases even after several cycles.[37,38] Based on the discussion that follows the peaks are assigned to phase transformations as shown in Table 1. The theoretical specific capacities, also given for comparison in Table 1, are consistent with these assignments.

The derivative Operando (dOp) NMR spectrum, shown in Fig. 3B, is obtained by taking the first derivative of the conventional NMR spectrum, shown in Fig. 3A, with respect to the operando time as described earlier.[27] The dOp NMR spectrum provides a clearer and richer view into the chemistry of the lithiation and delithiation processes. Positive derivative intensities are shown in green and represent formation of lithium species (henceforth called *formation resonances*) whereas negative derivative intensities are shown in red and represent the removal of lithium species (henceforth called *removal resonances*). Thus, a dOp NMR spectrum can reveal the removal of reactants and formation of products associated with a given reaction. For example, around $t_{op} \approx 35$ h we observe a formation resonance at ~80 ppm for a species A and a removal resonance at ~273 ppm for Li metal dendrites, both associated with the redox reaction of peak I. One must be careful interpreting dOp NMR spectra as partial or complete destructive interference from strong overlap of removal and formation

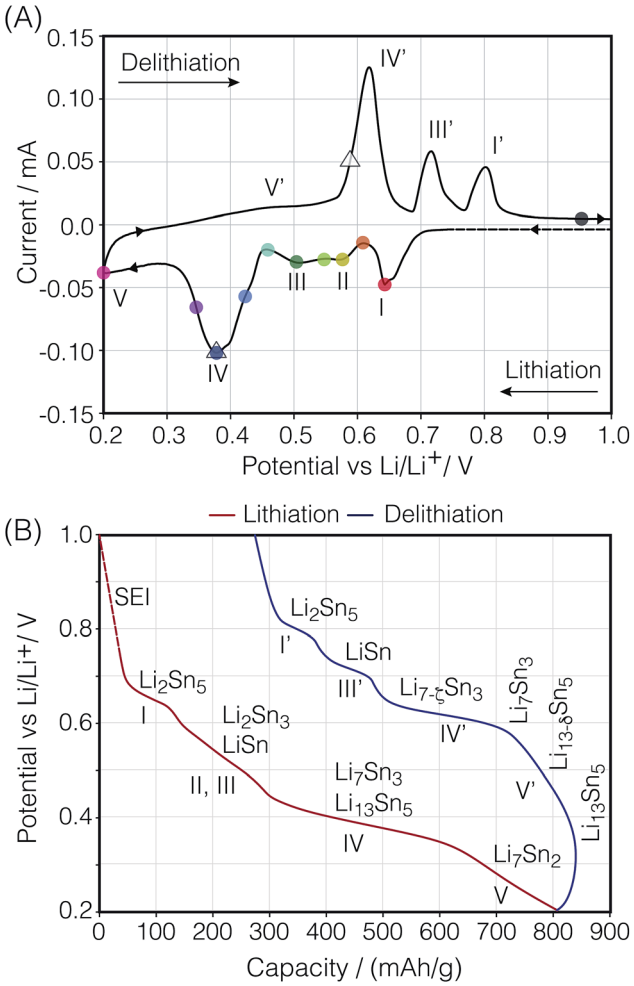

Fig. 2 (A) Cyclic voltammogram of the fourth cycle of the Sn/Li electrochemical cell depicting lithiation as a function of potential at 2.5 μV s^{-1}. Not shown: first 3 CV cycles of fresh Sn electrode at 1 mV s^{-1}. The colored dots mark the potentials where the *ex situ* ^{7}Li MAS NMR spectra in Fig. 4 were measured. The triangles mark the potentials where the *ex situ* pair distribution functions were measured. (B) Specific capacity during the fourth cycle of the cell as a function of cell potential.

resonances can occur and hide the existence of some species participating in the reaction. Thus, it is also useful to track which conventional NMR resonances have been removed by the dOp transform.[27] Generally, we find the dOp intensities of the lithium metal dendrite resonances to be well correlated to the CV current. The drop and disappearance of lithium metal signal intensity (and disagreement with the CV current) at $t_{op} \approx 75$ h in Fig. 3B, however, corresponds to the situation where there has been a complete removal of deposited lithium dendrites on the counter electrode during lithiation of the Sn anode. It is not until $t_{op} \approx 125$ h, during delithiation, that the lithium metal dendrite resonances reappear. As long as lithium dendrites are present on the counter electrode, we observe that the intensities of the lithium metal resonances in the dOp spectrum are correlated to the CV current.

For comparison, Fig. 3C shows the CV current as a function of operando time (solid black line), the partial projection over

Table 1 Theoretical and experimental cell specific capacity during the different stages of lithiation and delithiation of a Sn electrode containing 2.84 mg of active Sn. See main text for details on the assignments

	CV Peak/ region	Assignment	Δx	E integration limits (V)	Experimental (mA h g^{-1}) ΔQ	Experimental (mA h g^{-1}) Q	Theoretical (mA h g^{-1}) ΔQ	Theoretical (mA h g^{-1}) Q
	SEI	SEI	-	$1.0 \rightarrow 0.72$	40.4	40.4	0	0
Lithiation Li_xSn formation	I	$Sn \rightarrow Li_2Sn_5$	0.4	$0.72 \rightarrow 0.61$	96.8	137.2	90.3	90.3
	II	$Li_2Sn_5 \rightarrow Li_2Sn_3^*$	$0.2\overline{6}$	$0.61 \rightarrow 0.55$	55.5	192.2	60.2	150.5
	III	$Li_2Sn_3^* \rightarrow LiSn$	$0.\overline{3}$	$0.55 \rightarrow 0.45$	102.6	294.7	75.3	225.8
	IV	$LiSn \rightarrow Li_7Sn_3$	$1.\overline{3}$	$0.45 \rightarrow 0.30$	397.1	685.9	361.2	587.0
	IV	$Li_7Sn_3 \rightarrow Li_{13}Sn_5$	$0.2\overline{6}$					
	V	$Li_{13}Sn_5 \rightarrow Li_7Sn_2$	0.9	$0.30 \rightarrow 0.2 \rightarrow 0.32$	156.5	842.4	203.2	790.2
Delithiation Li_xSn removal	V′	$Li_7Sn_2 \rightarrow Li_{13}Sn_5$	0.9	$0.32 \rightarrow 0.50$	63.6	778.9	203.2	587.0
	IV′	$Li_{13}Sn_5 \rightarrow Li_7Sn_3$	$0.2\overline{6}$	$0.50 \rightarrow 0.69$	296.4	482.5	361.2	225.8
	IV′	$Li_7Sn_3 \rightarrow LiSn$	$1.\overline{3}$					
	III′	$LiSn \rightarrow Li_2Sn_5$	0.6	$0.69 \rightarrow 0.77$	97.8	384.7	135.5	90.3
	I′	$Li_2Sn_5 \rightarrow Sn$	0.4	$0.77 \rightarrow 1.0$	108.6	276.1	90.3	0.00

the lithium metal dOp NMR resonance at 274 ppm (rate of dendrite removal and formation) as a dashed blue line, and the partial projection over the Li_xSn resonances in the region from −50 ppm to 150 ppm as the dashed red line. Note, to follow the IUPAC convention that reduction currents are negative we invert the sign of the dOp NMR projections.

3.1 Peak I

Beginning at operando time, $t_{op} = 0$ h ($E_{op} = 1.0$ V), the first evidence of intermetallic formation, peak I, occurs at $t_{op} = 34.7$ hc($E_{op} = 0.69$ V), where a resonance at 80 ppm appears. This formation resonance is assigned to the formation of the intermetallic phase Li_2Sn_5,

$$\text{Peak I: Sn} + 0.40\text{Li}^+ + 0.40\text{e}^- \rightarrow 0.20\text{Li}_2\text{Sn}_5, \quad (1)$$

and had previously been assigned by operando X-ray measurements.[6,11] Further support for this assignment is found in the *ex situ* ^{7}Li NMR magic-angle spinning (MAS) spectra shown in Fig. 4. These spectra were acquired at the series of potentials shown in the far right, and indicated on the CV in Fig. 2A by the colored dots.

The *ex situ* ^{7}Li NMR MAS spectrum of the electrode cycled to peak I (0.62 V) is shown in Fig. 4A. The sharp and broad resonances near 0 ppm are assigned to the electrolyte and SEI, respectively. The resonance at 76.1 ppm is assigned to Li_2Sn_5. This phase has the largest Knight shift of the observed Li_xSn phases in this study, and is consistent with previous NMR measurements.[36,39,40] In ^{7}Li NMR measurements on a series of liquid Li–Sn alloys van der Marel *et al.*[39] found, with increasing addition of Sn to Li, that the ^{7}Li Knight shift falls rapidly from 265 ppm in pure lithium metal to a minimum of 60 ppm in the Li_4Sn alloy, and then rises to about 110 ppm in the lower Li–Sn ratio alloys. In solid Li–Sn alloys Furuya *et al.*[40] found that the ^{7}Li NMR Knight shift follows a similar pattern with the minimum ^{7}Li NMR Knight shift occurring in the Li_7Sn_2 alloy. Assuming that the Fermi contact interaction between the nucleus and the electron spins is the dominant contribution, the Knight shift is given by

$$K = \frac{8\pi}{3}\Omega\chi_p P_F, \quad (2)$$

where Ω denotes the average atomic volume, χ_p the Pauli spin susceptibility and P_F a Fermi surface average of the electron contact density at the ^{7}Li nucleus. Starting with this expression, van der Marel *et al.*[39,41] showed that the decrease in ^{7}Li Knight shift is primarily due to a decrease in the spin susceptibility, χ_p, which in turn can be related to the change in the alloy resistivity that dramatically peaks around the composition Li_4Sn. Bekaert *et al.*[36] prepared the seven Li–Sn crystalline phases known from the binary phase diagram, Li_2Sn_5, LiSn, Li_7Sn_3, Li_5Sn_2, $Li_{13}Sn_5$, Li_7Sn_2, and $Li_{22}Sn_5$ by ball-milling, and measured their ^{7}Li MAS NMR spectra. They similarly found that the ^{7}Li Knight was proportional to the density of states at the Fermi level.

3.2 Peaks II and III

Peaks II and III appear at 0.57 V and 0.51 V, respectively. In the dOp spectrum at peak II a formation resonance labeled B appears along with a correlated removal resonance for the Li metal dendrites. There is, however, no apparent removal of resonance A (Li_2Sn_5). At peak III we observe a formation resonance labeled C with a correlated removal resonance for B and a lower removal resonance for the Li metal dendrites.

Turning to the *ex situ* ^{7}Li MAS NMR spectra in Fig. 4C–F we see that the LiSn phase distinctly appears as two resonances at 32 and 42 ppm. The relatively narrow NMR line widths observed for LiSn is attributed to two non-exchanging Li crystallographic sites present in this phase based on the work by Bekaert *et al.*[36]

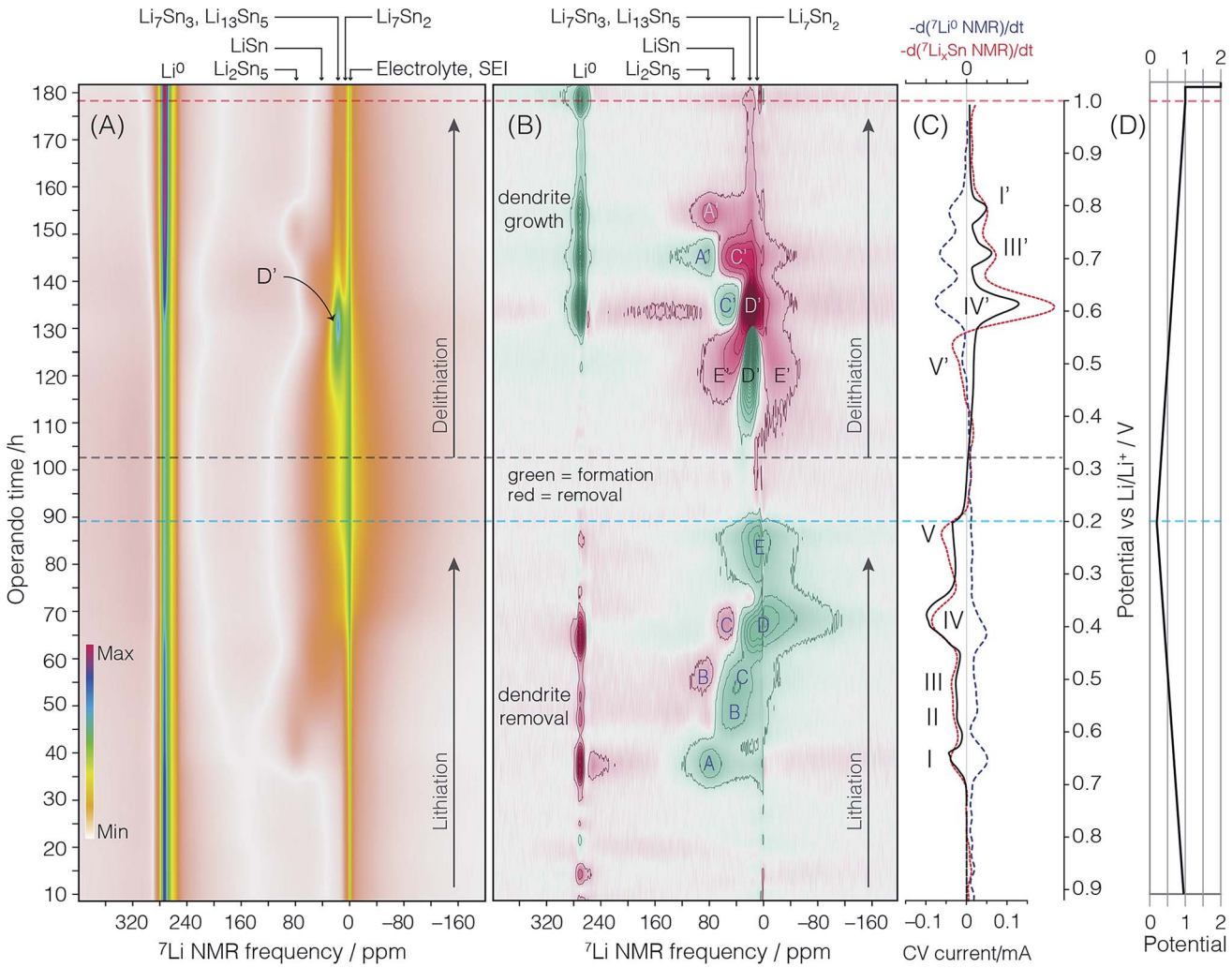

Fig. 3 (A) 2D ^{7}Li NMR color intensity plot of the 4th cycle at a sweep rate of 2.5 μV s^{-1} showing the relative signal intensities as a function of time. The first 3 cycles starting with a fresh Sn electrode were swept at 1 mV s^{-1}. The horizontal axis is the NMR frequency shift *vs.* a 1 M LiCl reference, the *y*-axis is the operando time in hours during the cycle. The horizontal blue dashed line represents the time at which the current polarity was switched and the red dashed line represents the end of the 4th cycle. (B) ^{7}Li dOp NMR spectrum. In (A) color map hue is linearly proportional to intensity, and in (B) green and red represents positive and negative amplitudes, respectively. In both plots the color saturation goes to zero as the intensity magnitude approach zero. (C) Cell potential as a function of operando time. (D) Cell potential as a function of time.

The LiSn resonances in the *ex situ* ^{7}Li MAS NMR spectra continue to grow up to 0.47 V and, based on the total charge needed to form LiSn, its formation is complete at the onset potential of peak IV.

While evidence of LiSn formation is apparent beginning at 0.56 V and at lower potentials in the *ex situ* ^{7}Li MAS NMR spectra of Fig. 4, at the same potentials we also see evidence of broad ^{7}Li resonances in the base line underlying the narrow Li_2Sn_5 resonance, labeled B. These resonances seem to arise from a highly disordered phase with a Knight shift that is intermediate between Li_2Sn_5 and LiSn. Given the *ex situ* ^{7}Li MAS evidence for a spectrally broad B resonance, the curious lack of a removal resonance for A at peak II during the formation of B in the dOp spectrum could be the result of destructive interference of an overlapping removal resonance for A and the broader formation resonance for B. Using coulometric titration Wang *et al.*[42] observed the formation of a phase with stoichiometry $Li_{0.7}Sn$ between Li_2Sn_5 and LiSn. Using *ab initio* random structure searching Morris and coworkers[43] recently predicted three metastable phases between Li_2Sn_5 and LiSn, of which Li_2Sn_3 is the closest to the hull and the $x = 0.7$ composition determined by Wang *et al.*[42] One might speculate that resonance B could possibly be associated with the metastable Li_2Sn_3 phase, but further work would be needed for a more definitive assignment. On this basis, we tentatively assign peak II to the formation of Li_2Sn_3,

$$\text{Peak II: } 0.20Li_2Sn_5 + 0.27Li^+ + 0.27e^- \rightarrow 0.\bar{3}Li_2Sn_3. \quad (3)$$

And peak III to the formation of LiSn,

$$\text{Peak III: } 0.\bar{3}Li_2Sn_3 + 0.33Li^+ + 0.33e^- \rightarrow LiSn. \quad (4)$$

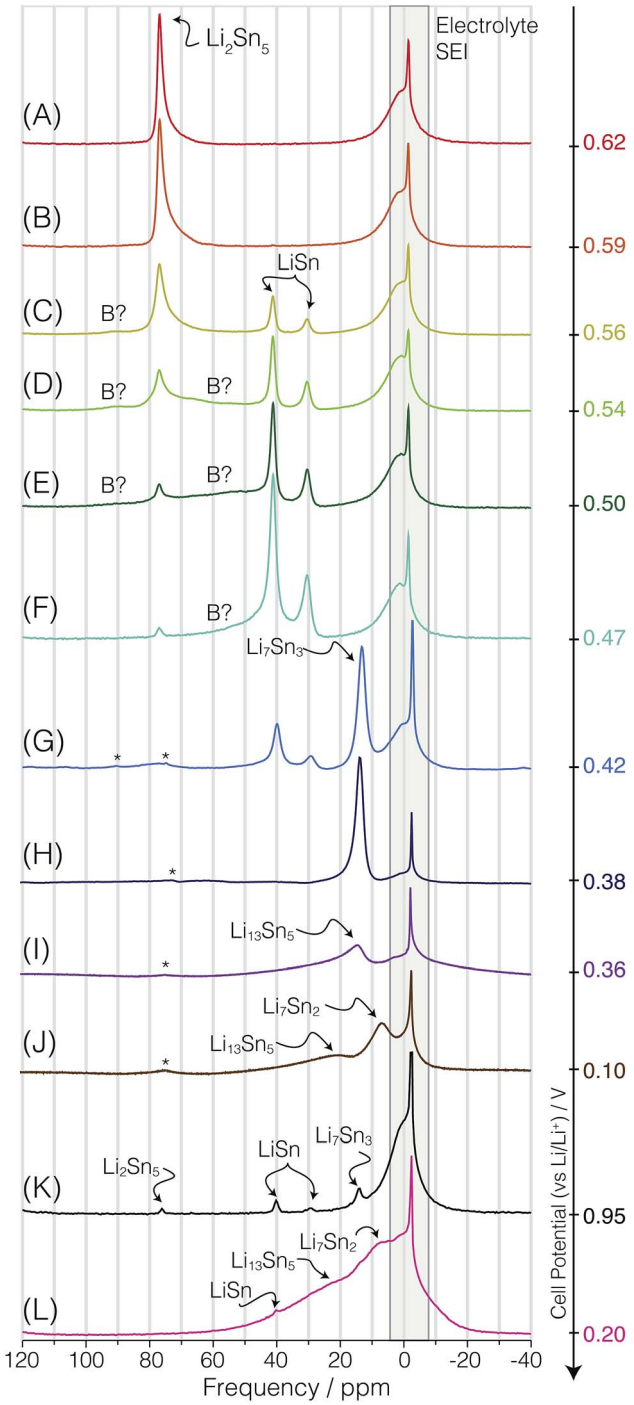

Fig. 4 *Ex situ* ^{7}Li MAS NMR spectra of different Sn electrodes lithiated at 2.5 μV s^{-1} to potentials of (A) 0.62 V, (B) 0.59 V (C) 0.56 V, (D) 0.54 V, (E) 0.50 V, (F) 0.47 V, (G) 0.42 V, (H) 0.38 V, (I) 0.36 V, (J) 0.10 V, (K) delithiation to 0.95 V, and (L) relithiation to 0.20 V. All spectra were measured on cells during the 1st cycle except (L) which was measured on a cell relithiated during the 2nd cycle. The MAS spinning speed is 20 kHz for all spectra except (G), (H), (I), and (J) where it is 12 kHz. Spinning sidebands are marked with asterisks.

3.3 Peak IV

Further lithiation during peak IV at $t_{op} = 64.5$ h ($E_{op} = 0.42$ V) results in a removal resonance for C (LiSn), while a broad dOp NMR formation resonance, labeled D, appears. Based primarily on first principles calculations,[51] peak IV is generally associated with the formation of Li_7Sn_3, Li_5Sn_2 and $Li_{13}Sn_5$, which are structurally very similar and hardly distinguishable in the XRD. As the Knight shifts of these three phases are similar,[36,40] we do not expect them to be resolved in the NMR spectrum using static conditions. The observed shift of the resonance labeled D at ~17 ppm is consistent with these earlier measurements. At potentials below $E_{op} = 0.4$ V the dOp NMR CV in Fig. 3C indicates the intensity of the formation resonance labeled D is less than expected from the current. This, however, is likely due to differences in ^{7}Li spin–lattice relaxation times, T_1 for these phases, (see Table S1†), leading to some differential magnetization recovery of all ^{7}Li and a relatively lower intensity.

The Li_7Sn_3, Li_5Sn_2 and $Li_{13}Sn_5$ phases appear as one resonance at 13.2 ppm at 0.47 V in the *ex situ* ^{7}Li MAS NMR spectrum in Fig. 4G, shifting to 14.2 ppm in Fig. 4I at 0.36 V. A significant difference between lithium mobilities in LiSn and the Li_7Sn_3, Li_5Sn_2 and $Li_{13}Sn_5$ phases is apparent in the *ex situ* MAS NMR spectra of Fig. 4C–G and G–I. As noted by Bekaert *et al.*,[36] while two distinct ^{7}Li resonances are observed for LiSn, corresponding to its two crystallographically distinct sites, only one ^{7}Li resonance is observed for Li_7Sn_3 even though it contains 7 crystallographically distinct sites, again suggesting that a higher Li mobility in Li_7Sn_3 leads to fast exchange among sites on the NMR time scale.

To elucidate further the structures responsible for resonance D, *ex situ* pair distribution function (PDF) measurements, shown in Fig. 5, were performed on samples obtained in the first cycle of cells lithiated to the potential, 0.38 V, marked with a triangle in Fig. 2A, where resonance D is formed. We note that the PDF of the resonance D sample is composed of sharp, intense peaks, indicating the presence of nanoclusters with well defined structures.[52] The data was fitted to the known phases by performing refinements of lattice parameters, non-special angles, isotropic atomic displacement parameters, Sn correlated motion, and scaling factors for nanoparticles with a 60 nm diameter to obtain information about the local structure of both transitions. The fit of the PDF of the resonance D sample to three Li_xSn phases (Li_7Sn_3, Li_5Sn_2, and $Li_{13}Sn_5$) between 2 and 15 Å is also shown in Fig. 5. The fit resulted in a combination of two phases, Li_7Sn_3 and $Li_{13}Sn_5$, with stoichiometric amounts of

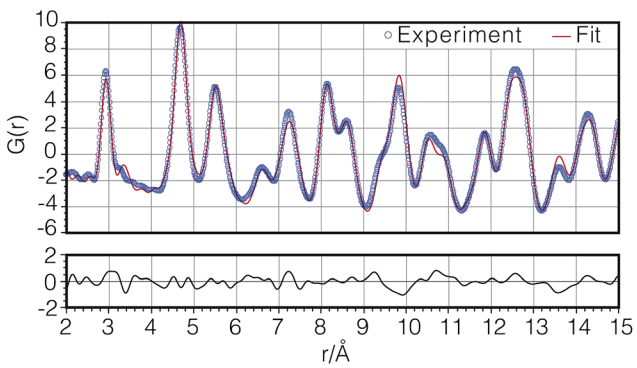

Fig. 5 The pair distribution function of a sample obtained in the first cycle of a cell cycled to the potential where peak D is formed and its best fit. $R_w = 0.13$.

61.1% and 38.9% respectively, and unit cell parameters given in Table 2. The unit cell parameters obtained for both Li_7Sn_3 and $Li_{13}Sn_5$ remained within 2% of the literature values. It is noteworthy that Li_5Sn_2, being the intermediate phase between Li_7Sn_3 and $Li_{13}Sn_5$, gives no contribution to the fit. This phase has been previously synthesized by chemical alloying[36,48] and is known to be metastable.[43] The absence of this phase during lithiation suggests that the electrochemically formed Li_5Sn_2 is short lived or that it cannot be formed electrochemically.

On the basis of the NMR and PDF measurements we assign peak IV to the reactions

$$\text{Peak IV}: \begin{cases} \text{LiSn} + 1.33\text{Li}^+ + 1.33\text{e}^- \rightarrow 0.\bar{3}\text{Li}_7\text{Sn}_3, \\ 0.\bar{3}\text{Li}_7\text{Sn}_3 + 0.27\text{Li}^+ + 0.27\text{e}^- \rightarrow 0.2\text{Li}_{13}\text{Sn}_5. \end{cases} \quad (5)$$

3.4 Peak V

Peak V is observed at $t_{op} = 76.5$ h and ($E_{op} = 0.31$ V). Here a broad formation resonance, labeled E, about 160 ppm appears in the dOp spectrum centered at 9.5 ppm. At this point in the lithiation cycle all the lithium dendrites have been removed, so associated removal resonance at the Li metal resonance position is not seen. Furthermore, because of the strong overlap of D and E, no removal resonance for D is observed. Examining the *ex situ* ^{7}Li MAS NMR spectra in Fig. 4J we observe a resonance at 6.8 ppm, which is similar to the resonance assigned by Furuya *et al.*[40] and Bekaert *et al.*[36] to Li_7Sn_2. Thus, we assign peak V to the reactions

$$\text{Peak V}: 0.2\text{Li}_{13}\text{Sn}_5 + 0.90\text{Li}^+ + 0.90\text{e}^- \rightarrow 0.5\text{Li}_7\text{Sn}_2. \quad (6)$$

The intensity of E increases until the cell reaches the end of lithiation at $t_{op} = 89$ h ($E_{op} = 0.20$ V) and remains almost unchanged even when the cell potential is reversed during the first hours of delithiation at $t_{op} = 92$ h ($E_{op} = 0.27$ V). At 0.2 V, however, the conversion of $Li_{13}Sn_5$ to Li_7Sn_2 is incomplete, and the electrode at the end of the lithiation cycle is a mixture of these two phases. At $t_{op} = 89$ h, when the cell potential reaches 0.2 V, the polarization direction is reversed and remains reductive to 0.32 V. During this period there are no formation nor removal resonances in the dOp NMR spectrum.

3.5 Peak V′

Oxidative electrochemical current, *i.e.*, delithiation of Li_xSn, begins at $t_{op} = 102.5$ h ($E_{op} = 0.32$ V). At this point in the dOp spectrum we observe the simultaneous appearance of a broad removal peak E′ (Li_7Sn_2) along with a narrow formation resonance labeled D′ at ~16 ppm. We see a notable difference in line widths with the resonance D′ for peak V′ during delithiation being substantially narrower than the resonance labeled D for peak V during lithiation. Despite the increase in sensitivity of D′ over D the total integrated area of all Li resonances, *i.e.*, Li metal and Li_xSn, remains relatively constant throughout lithiation and delithiation. The D′ resonance reaches a resonance height about 5.6 times higher than that of D during lithiation. The most likely explanation for the narrowing of the D′ line width is due to a lithium vacancy rich phase with an increased lithium mobility and an averaging of NMR shifts over different lithium sites on a time scale faster than the NMR measurement. This narrow D′ begins at 0.32 V and is likely due to formation of an $Li_{13}Sn_5$ phase which is rich in lithium vacancies. This narrow resonance continues to grow to 0.58 V at which point it starts to decrease. At this potential, however, this resonance is likely associated with a vacancy rich Li_7Sn_3 phase, which has a nearly identical Knight shift as $Li_{13}Sn_5$.

The fraction of the Li_xSn sites responsible for the D′ resonance remain stable at higher potentials, and accumulates over multiple cycles. This is clearly seen in the operando ^{7}Li NMR spectrum of a cell that has been cycled through 11 cycles at a sweep rate of 50 μV s^{-1}, shown in Fig. 6. On the far left in Fig. 6 are two expanded regions of the NMR spectrum comparing the region where D′ is formed and removed during the first and seventh cycle. At the end of the seventh cycle a significant

Table 2 At the top are fractional compositions and unit cell parameters determined by pair distribution function measurements on cells cycled to the potentials, 0.38 V (lithiation) and 0.58 V (delithiation), where resonances D and D′, respectively, are formed. At the bottom are the unit cell parameters from the literature for comparison

	Fract. comp.	Structure	a/Å	b/Å	c/Å	γ/°
D	0.611	Li_7Sn_3 (2 × 2 × 1)	9.42(18.85)	8.75(17.49)	4.72	106.3
	0.389	$Li_{13}Sn_5$	4.71	4.71	17.03	120
D′	0.857	$Li_{7-\zeta}Sn_3$	18.93	17.11	4.73	104.7
	0.143	LiSn	5.19	7.87	3.17	105.4

Structure	Space group	a/Å	b/Å	c/Å	γ/°	$\Delta V/V_{i-1}$	Ref.
β-Sn	$I4_1/amd$	5.83	5.83	3.18	90	—	44
Li_2Sn_5	$P4/mbm$	10.27	10.27	3.125	90	23%	45
LiSn	$P2/m$	5.17	7.74	3.18	104.5	24%	46
Li_7Sn_3	$P2_1/m$	9.45	8.56	4.72	106.0	49%	47
Li_5Sn_2	$R\bar{3}m$	4.74	4.74	19.83	90	21%	48
$Li_{13}Sn_5$	$P\bar{3}m1$	4.70	4.70	17.12	120	2%	49
Li_7Sn_2	$Cmmm$	9.80	13.80	4.75	90	6%	50

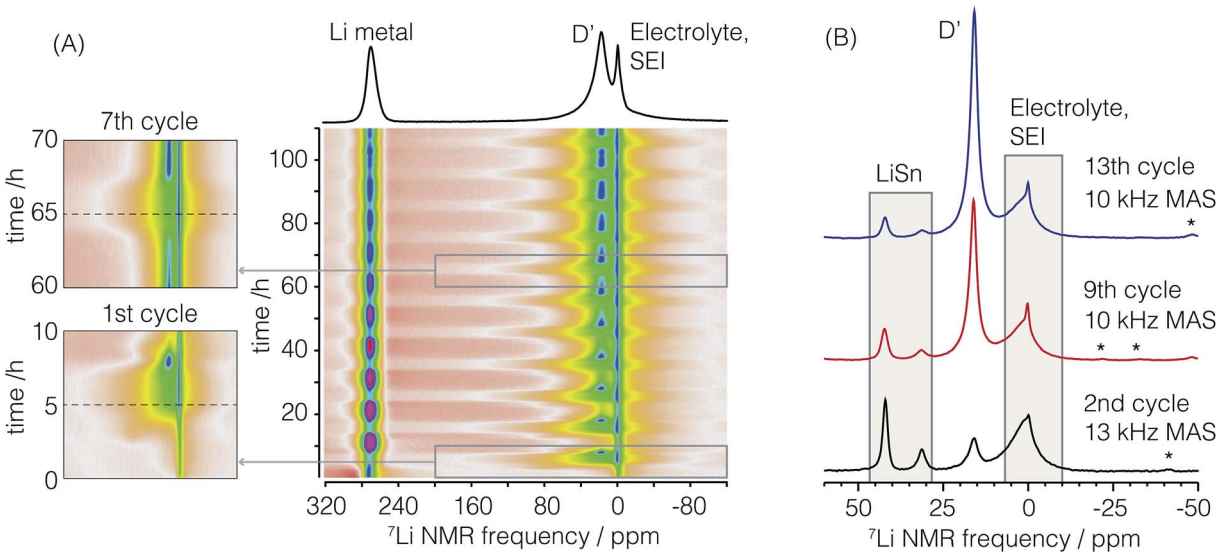

Fig. 6 (A) Operando ^{7}Li NMR 2D spectra of eleven cycles of a Sn electrode cell at a sweep rate of 50 μV s^{-1}. (B) *Ex situ* ^{7}Li MAS NMR spectra of Sn samples cycled to D′ at a sweep rate of 50 μV s^{-1} after 2 (black), 9 (red), and 13 (blue) complete cycles, lithiated to 0.2 V and then delithiated to 0.58 V to form D′. The MAS NMR of the cell at 2 cycles shows intense resonances at 42 and 32 ppm corresponding to the two non-exchanging crystallographic sites of LiSn, and a resonance at 15.8 ppm corresponding to the D′. As more cycles are performed, a decrease in the intensity of the LiSn resonance and an increase in the intensity of the D′ resonance is observed.

fraction of the D′ resonance clearly remains. A most interesting result is that the D′ resonance disappears every time the cell is fully lithiated, that is, at 0.1 V, and thus must still remain connected to the circuit to be re-lithiated. Thus, whatever Li_xSn phase is associated with D′ seems to be easily lithiated to Li_7Sn_2, but hindered from delithiation. The variation in the Li metal dendrite resonance intensity is consistent with this picture as it decreases during lithiation, but never grows as large during delithiation at the end of each cycle, that is, lithium becomes trapped in the phase associated with D′.

On the right in Fig. 6 are *ex situ* ^{7}Li MAS NMR spectra containing D′ for different cells cycled for 2 (black), 9 (red), and 13 (blue) complete cycles, and then lithiated to 0.2 V and delithiated to 0.58 V. The *ex situ* ^{7}Li MAS NMR spectrum of the cell at 2 cycles shows intense resonances at 42 ppm and 32 ppm corresponding to the two non-exchanging crystallographic sites of LiSn, and a resonance at 13.8 ppm, which is consistent with three phases, $Li_{13}Sn_5$, Li_5Sn_2 and Li_7Sn_3. As more cycles are performed, we clearly see a decrease in the intensity of the LiSn peaks and an increase in the intensity of the 13.8 ppm resonance, as seen previously in the operando NMR spectra.

To determine the structures responsible for resonance D′, *ex situ* pair distribution function (PDF) measurements were performed on samples obtained in the first cycle of cells delithiated to the potential 0.58 V (marked with a triangle in Fig. 2A), where resonance D′ is formed with highest intensity in the operando NMR spectrum. The result is shown in Fig. 7 as the solid blue line along with the PDF of D as a dashed black line. Compared to D, all PDF peaks in D′ are broader and lower in intensity. Notably, the PDF of D′ lacks a peak at 6.6 Å, which is due to an absence of $Li_{13}Sn_5$, and has an additional peak at 6.2 Å. Among the different crystal structures in the Li_xSn system, the only structure containing Sn–Sn atom distances around 6.2 Å is LiSn, a phase confirmed by *ex situ* ^{7}Li MAS NMR measurements (Fig. 6B) as co-existing with D′. The presence of LiSn is reasonable since it is the delithiation phase of Li_7Sn_3. To account for the NMR evidence of highly mobile Li in the phase associated with D′ the structural model for fitting the PDF included a 2 × 2 × 1 supercell of Li_7Sn_3 with the possibility of fractional occupancies of lithium sites. The best fit to the PDF employing this vacancy rich 2 × 2 × 1 supercell of $Li_{7-\zeta}Sn_3$ and the unit cell of LiSn is shown in Fig. 8. No further improvement to the fit was obtained with addition of $Li_{13}Sn_5$ and Li_5Sn_2 structures. Again, as noted earlier, it is likely that a vacancy rich $Li_{13}Sn_5$ phase is present at lower potentials in the delithiation cycle. Based on this analysis the relative abundance of the resulting vacancy rich $Li_{7-\zeta}Sn_3$ supercell with $\zeta = 1.6$ and LiSn are 85.7% and 14.3%, respectively, with a goodness of fit of 0.137. A comparison of the best fit unit cell parameters are given in Table 2. The unit cell parameters obtained for both $Li_{7-\zeta}Sn_3$ and LiSn remained within 2% of the literature values. A comparison of the Li_7Sn_3 structure of D and the vacancy rich

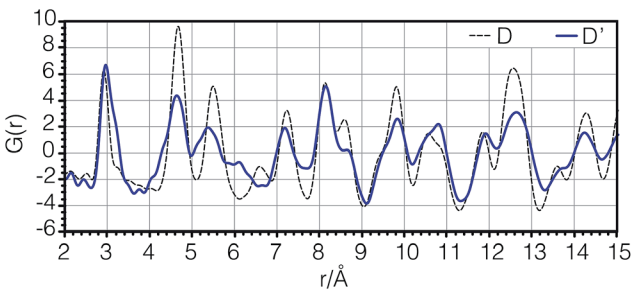

Fig. 7 Comparison of pair distribution functions between 2 and 15 Å obtained from the 1st cycle of cells cycled to resonance D and to D′ during lithiation and delithiation, respectively.

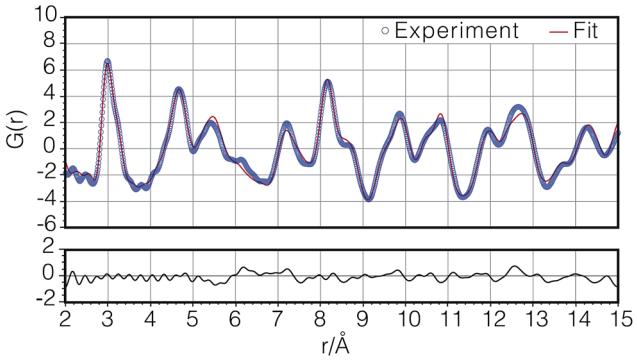

Fig. 8 The pair distribution function of a sample obtained in the first cycle of a cell cycled to the potential where peak D′ is formed and its best fit. $R_w = 0.14$.

$Li_{7-\zeta}Sn_3$ structure of D′, both from PDF analyses, are given in Fig. 9. The number of Li removed from the Li_7Sn_3 structure to achieve this fit is about 20%, which amounts to a Li : Sn ratio of 1.8. The formation potential of LiSn occurs between 0.61 V and 0.45 V, as seen in the CV of Fig. 3A, while the delithiation of Li_7Sn_3 occurs at 0.58 V. The formation of the $Li_{7-\zeta}Sn_3$, therefore, occurs at potentials at which it is also thermodynamically favorable to form LiSn.

To check the stability of the phases associated with D′ additional *in situ* ^{7}Li NMR measurements were performed on another cell cycled with a slow potential sweep of 2.5 μV s^{-1} from 0.2 to 0.58 V, where the D′ resonance at ∼16 ppm has the maximum intensity. This cell was then held at 0.58 V for 40 h and monitored with ^{7}Li NMR. During this period an 8% decay in the NMR signal of D′ was observed along with an associated formation of C′.

On this same cell, variable (low) temperature *in situ* ^{7}Li NMR spectra were measured starting from room temperature (298 K) down to 173 K in steps of 5 K. On a different but otherwise identical cell, variable (high) temperature *in situ* ^{7}Li NMR spectra were measured starting from room temperature (298 K) up to 403 K in steps of 10 K. These spectra are shown in Fig. S5A.† The static NMR line width of the D′ resonance increases with decreasing temperature, while the peak area remained constant—consistent with a reduction of Li mobility at lower temperatures. At 323 K the D′ resonance begins to diminish and the C′ (LiSn) resonance begins to grow. At the higher temperature of 373 K no D′ resonance remains and only the C′ (LiSn) resonance is observed.

Ex situ VT ^{7}Li MAS NMR spectra on $Li_{7-\zeta}Sn_3$ (Fig. S5B, ESI†) exhibit a narrower line width of 2.5 ppm at 303 K which increases to 4.6 ppm at 243 K. This suggests that the static line broadening at lower temperatures arises from a distribution of isotropic and anisotropic shifts, both of which are partially averaged away in the static spectrum by the increased Li mobility at room temperature.

Based on the NMR and PDF evidence we assign peak V′ to the reactions

$$\text{Peak V}' : \begin{cases} 0.5Li_7Sn_2 \rightarrow 0.2Li_{13}Sn_5 + 0.90Li^+ + 0.90e^-, \\ Li_{13}Sn_5 \rightarrow Li_{13-\delta}Sn_5 + \delta Li^+ + \delta e^- \\ \qquad\qquad \rightarrow 0.\bar{3}Li_7Sn_3 + 0.2\bar{6}Li^+ + 0.2\bar{6}e^-. \\ Li_7Sn_3 \rightarrow Li_{7-\zeta}Sn_3 + \zeta Li^+ + \zeta e^- \end{cases} \quad (7)$$

3.6 Peak IV′

During peak IV′ at 0.62 V we observe the partial removal of D′ ($Li_{7-\zeta}Sn_3$) and the correlated formation of C′ (LiSn) in the dOp spectrum. Thus, we assign peak IV′ to the reaction

$$\text{Peak IV}': 0.\bar{3}Li_{7-\zeta}Sn_3 \rightarrow LiSn + (1.\bar{3} - 0.\bar{3}\zeta)Li^+ + (1.\bar{3} - 0.\bar{3}\zeta)e^-. \quad (8)$$

3.7 Peak III′

During peak III′ at 0.72 V we observe removal of C′ (LiSn) and a correlated formation of Li metal dendrites and formation of A′ (Li_2Sn_5), although it is possible that it includes some B′ (Li_2Sn_3) formation as well. Unlike the CV current and the projection of the lithium metal dendrite dOp resonances during lithiation, where peak II was observed in between peaks I and III, during delithiation there is no evidence of a resolved peak II′. This doesn't imply there is no formation of B′ (Li_2Sn_3), particularly since its NMR resonance is broad and may not be visible in the spectrum due to strong overlap with C′ (LiSn) removal and A′ (Li_2Sn_5) formation. Thus, we assign peak III′ to the reaction

$$\text{Peak III}': LiSn \rightarrow 0.2Li_2Sn_5 + 0.6Li^+ + 0.6e^- \quad (9)$$

3.8 Peak I′

During peak I′ at 0.80 V we observe a correlated formation of Li metal dendrites and the removal of A′ (Li_2Sn_5). The NMR resonance intensity of Li_2Sn_5 is 29% smaller compared to the NMR resonance intensity of Li_2Sn_5 during lithiation. This reveals that only 71% of the lithiated material is delithiated back to pure Sn, which agrees with the integrated capacity loss of 31%. At the end of the cycle at $t_{op} = 178$ h ($E_{op} = 1.0$ V) some residual $Li_{7-\zeta}Sn_3$ can still be observed in the spectrum, indicating that lithium in this phase remains trapped within the structure and is not removed from the electrode. Finally, we assign peak I′ to the reaction

$$\text{Peak I}': 0.2Li_2Sn_5 \rightarrow Sn + 0.4Li^+ + 0.4e^-. \quad (10)$$

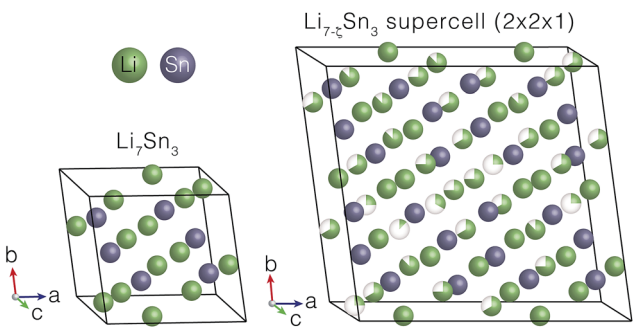

Fig. 9 Comparison of Li_7Sn_3 and $Li_{7-\zeta}Sn_3$ structures obtained from PDF analysis of cells cycled to resonance D and to D′ during lithiation and delithiation, respectively.

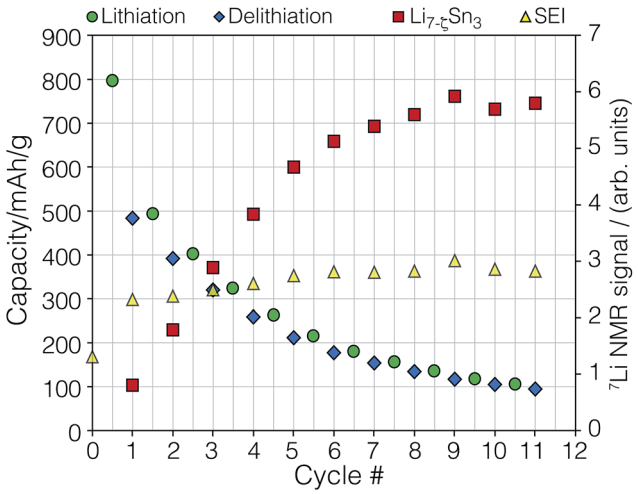

Fig. 10 Comparison of cell capacity, NMR resonance intensity of SEI, and residual $Li_{7-\zeta}Sn_3$ at the end of each cycle, for a cell swept at 50 μV s^{-1}.

From 0.85 V to 1.0 V there is a low but constant dOp NMR formation resonance for the lithium metal dendrites as well as a correlated low and constant dOp NMR removal resonance for $Li_{7-\zeta}Sn_3$. Fig. 4K shows the *ex situ* MAS spectrum of a fully delithiated cell at the end of 1st cycle at 0.95 V. An important clue in the loss of cell capacity is the presence of resonances associated with the phases Li_2Sn_5, LiSn and $Li_{7-\zeta}Sn_3$ with relative integrated peak intensities of 2 : 13 : 29, respectively.

In an attempt to completely delithiate the Sn electrode, the cell was held at 1.0 V for 3 h and then at 2.0 V for another 1 h. Although there is a boost in the dOp metal dendrite formation resonance there is no significant dOp removal resonance of $Li_{7-\zeta}Sn_3$. The boost in the dOp metal dendrite formation resonance is correlated to electrolyte or SEI oxidation which is also observed at 0 ppm at t_{op} = 183 h.

3.9 Mechanism for capacity fade

The lithiation and delithiation cell capacities as a function of cycle number is shown in Fig. 10 as green and blue symbols, respectively. There is ∼30% cell capacity loss in each cycle. Shown as red squares in Fig. 10 are the $Li_{7-\zeta}Sn_3$ NMR resonance intensities at ∼16 ppm at the end of each cycle. There is a clear correlation to the capacity fade – increasing by 30% with each cycle. It is also worth mentioning that while the NMR intensity at −5 ppm for the SEI (yellow triangles in Fig. 10) increases significantly during the first cycle (∼78%), it grows slowly during the remaining 10 cycles (1–5% per cycle).

Conventional wisdom is that capacity fade in intermetallic anodes arises from particle cracking due to large volume expansions on lithiation. Such cracking during expansion has indeed been observed in TEM[53] and X-ray tomography[16] studies of micron sized Sn and Si particles on lithiation. Nanosized particles, however, are known to accommodate large stress and strain of volume changes during lithiation and delithiation without cracking.[8,12,19] The capacity fade in Fig. 10 shown as a function of half and full cycles, exhibits an odd behavior which seems inconsistent with simple cracking.

The capacity at the end of the first lithiation of our Sn nanoparticle (60 nm) electrode in Fig. 10 is close to the expected capacity of ∼740 mA h g^{-1}. This is calculated from the mass of Sn in the electrode, assuming lithiation to $Li_{13}Sn_5$ and then 75% conversion to Li_7Sn_2 when the lithiation of the cell is stopped at 0.2 V. The additional current can be assigned to SEI formation. On this basis alone one might believe the nanosizing of the Sn was successful in preventing cracking of the electrode during lithiation.

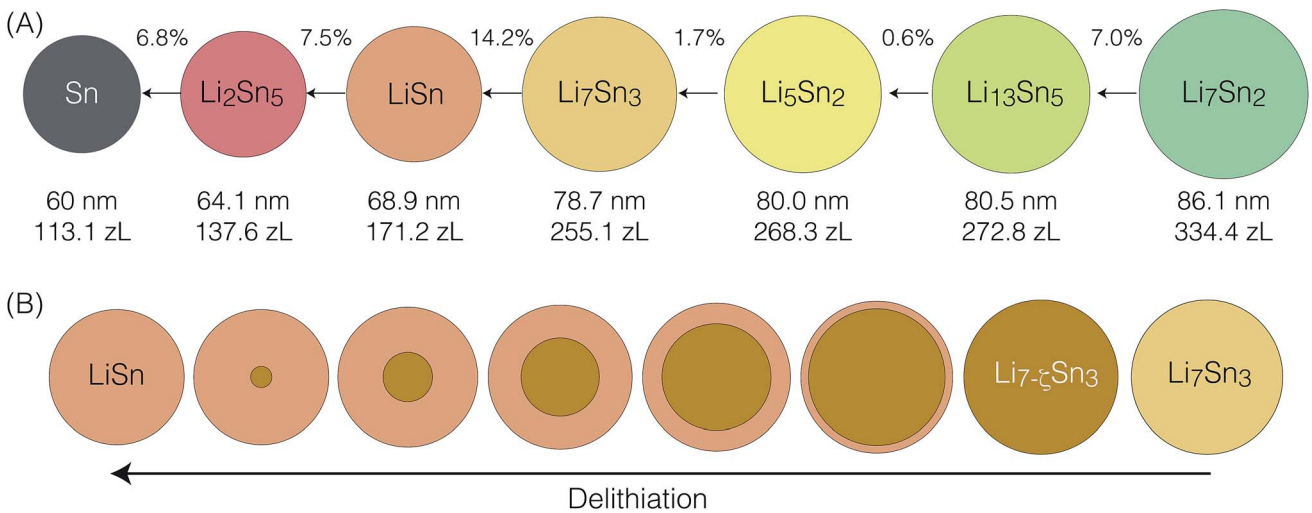

Fig. 11 (A) Illustration of particle size changes between Li_xSn phases found in the thermodynamic phase diagram. The percent particle diameter change on contraction (delithiation) is given above each arrow. Particles can disconnect at any stage of the delithiation process, but are more likely to disconnect during the largest volume changes. Individual particles can even disconnect before a given phase transition is complete. (B) Illustration of the phase coexistence inside a nanoparticle during delithiation from Li_7Sn_3 to LiSn, which undergoes the largest volume decrease. We assume that LiSn nucleation and growth begins at the particle surface where lithium are being removed, and expands into the center of the particle.

At the end of delithiation in the first cycle, however, we find the maximum capacity reduced by ~30% to 483 mA h g^{-1}. Perhaps more puzzling is that at the end of the second lithiation the capacity is 494 mA h g^{-1}, that is, no additional capacity fade is observed. This pattern of capacity fade during delithiation and no additional fade during lithiation is present in every cycle. This behavior appears opposite with the cracking behavior observed in micron sized particles, where cracking and a capacity fade is attributed to the lithiation process.[16] An important clue for explaining the capacity fade of the Sn nanoparticle electrode is that the operando NMR measurements show one particular phase, a vacancy rich $Li_{7-\zeta}Sn_3$, is only partially delithiated into LiSn. This phase not only remains present at the end of each cycle, but grows in intensity by the end of each cycle in a manner correlated to the capacity loss.

As illustrated in Fig. 11A there is a ~14% decrease in diameter during the Li_7Sn_3 to LiSn transition which is significantly larger than the ~7% or smaller diameter changes of the other phase transitions in the Li–Sn system. A possible explanation for the accumulation of $Li_{7-\zeta}Sn_3$ is that particles are disconnecting from the circuit, that is, the carbon/PVDF binder, before this particular delithiation step is complete—leaving particles in random states of delithiation along the transformation path shown in Fig. 11B. Consistent with this picture is the accumulation of the lower lithiated phases, Li_2Sn_5 and LiSn, also observed at the end of the delithiation cycle in the *ex situ* MAS spectrum of Fig. 4K.

A particularly curious additional piece of evidence in operando NMR spectrum of Fig. 6A is that the $Li_{7-\zeta}Sn_3$ resonance present at the end of each cycle disappears every time the cell is fully lithiated, that is, at 0.2 V. This is also consistent with an *ex situ* ^{7}Li MAS NMR spectrum, shown in Fig. 4K, obtained from a cell fully cycled and relithiated to 0.2 V. Here, the narrow resonance associated with disconnected $Li_{7-\zeta}Sn_3$-containing

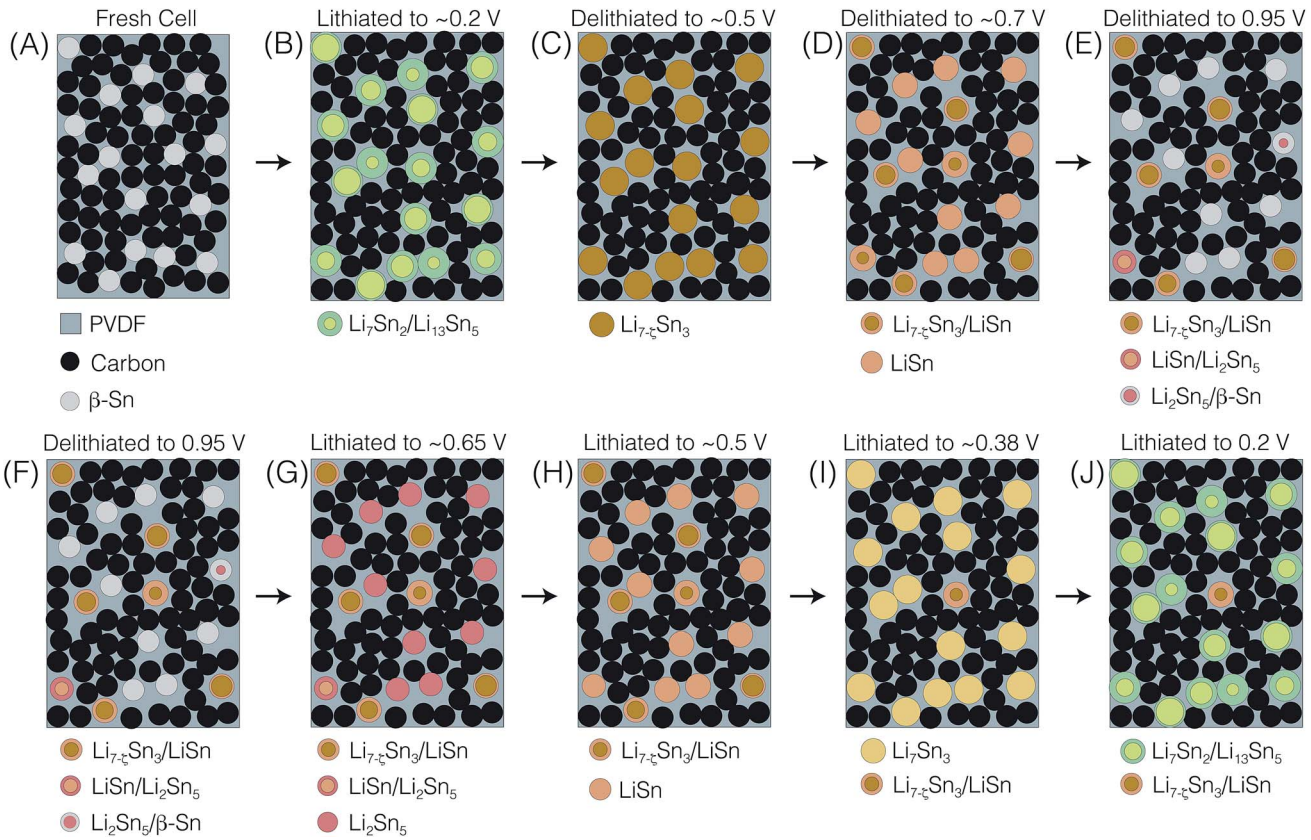

Fig. 12 The disconnection–reconnection hypothesis. In (A)–(E) is a 2D illustration of various electrode states during 1st cycle. In (A) is a fresh cell with a mixture of random close packed β-Sn, carbon black nanoparticles and PVDF in an approximate volume ratio of 17 : 75 : 8, respectively. In (B) is a depiction of the cell at the end of lithiation showing the expanded Li_xSn particles as mixtures of the Li_7Sn_2 and $Li_{13}Sn_5$ phases. In (C) is a depiction of the electrode after delithiation to ~0.5 V where the nanoparticles are primarily in the vacancy-rich phase, $Li_{7-\zeta}Sn_3$. In going from (B) to (C) the particle diameters decrease by ~2%. In (D) is a depiction of the electrode after delithiation to ~0.7 V where the LiSn nanoparticles begin forming. It is during this transition, where the nanoparticles' diameter decrease by ~14%, that particles lose electrical contact from the carbon black—stuck in various stages of delithiation between $Li_{7-\zeta}Sn_3$ and LiSn. In (E) is a depiction of the electrode at the end of delithiation to 0.95 V, where the process of particle disconnection continues with particles stuck in various stages of delithiation between LiSn and Li_2Sn_5, and Li_2Sn_5 and Sn. In (F)–(J) is a 2D illustration of various electrode states during lithiation of the 2nd cycle. In (F) is the electrode in the same state as (E). In (G) is an illustration of the electrode state after lithiation to ~0.65 V where all Sn particles have been lithiated to Li_2Sn_5 while the previously disconnected LiSn/Li_2Sn_5 begin reconnecting to the carbon black and $Li_{7-\zeta}Sn_3$/LiSn particles remain disconnected. In (H) the LiSn/Li_2Sn_5 particles have fully reconnected and converted into LiSn while the $Li_{7-\zeta}Sn_3$/LiSn particles begin reconnecting to the carbon black. In (I) and (J) the majority of particles are connected to the carbon black and become lithiated to Li_7Sn_3 and $Li_{13}Sn_5$/Li_7Sn_2, respectively.

particles is notably absent, and we see the clear presence of resonances from $Li_{13}Sn_5$ and Li_7Sn_2. This implies that these disconnected $Li_{7-\zeta}Sn_3$-containing particles somehow reconnect to the circuit and get fully relithiated into $Li_{13}Sn_5$ and Li_7Sn_2.

One hypothesis to explain this partial "healing" ability is that the volume expansion of particles during lithiation pushes the carbon/PVDF binder back into contact with the previously disconnected particles. This process is illustrated in Fig. 12. It is these reconnected particles that lead to the odd behavior, seen in Fig. 10, of no loss in lithiation cell capacity compared to the previous delithiation capacity. On delithiation, however, these reconnected particles become disconnected from the circuit, along with other newly disconnected particles. While particles can disconnect during any delithiation phase transition, the *ex situ* MAS spectrum in Fig. 4K suggests that the phase transitions with the larger diameter decreases are the more likely particles to lose contact, with the Li_7Sn_3 to LiSn transition being the most likely. It should be noted, however, that the NMR observation of $Li_{7-\zeta}Sn_3$ is facilitated by its narrow static ^{7}Li NMR line width. The continuing loss of capacity with increasing cycles implies that the number of disconnecting particles continue to grow.

4 Summary

We have performed extensive ^{7}Li operando NMR measurements along with selected *ex situ* ^{7}Li MAS NMR and PDF measurements to follow the electrochemical lithiation and delithiation of 60 nm Sn nanoparticles. We emphasize that the combination of thermodynamically controlled CV experiments with dOp NMR spectroscopy is an exciting new approach that clearly reveals more detailed information about structure and reactivity than conventional operando NMR spectra.

Cycling the cell with an ultra-slow sweep rate of 2.5 $\mu V\ s^{-1}$ to maintain a quasi-equilibrium throughout the processes we observe a series of intermetallic phases from β-Sn to Li_7Sn_2 and back. While these phases are somewhat consistent with the structural evolution of Li–Sn phases expected from the equilibrium binary phase diagram, there are some notable exceptions. During lithiation we observed evidence for a highly disordered phase having a Knight shift intermediate between Li_2Sn_5 and LiSn, which we speculate could be a metastable Li_2Sn_3 phase. This phase is consistent with stoichiometry $Li_{0.7}Sn$ observed between Li_2Sn_5 and LiSn in a coulometric titration by Wang *et al.*[42] Furthermore, based on analysis of PDF measurements, we did not find evidence for the electrochemical formation of Li_5Sn_2, the intermediate phase between Li_7Sn_3 and $Li_{13}Sn_5$ during lithiation and delithiation. During delithiation of Li_7Sn_2 a significantly narrow resonance for $Li_{13}Sn_5$ and Li_7Sn_3 appears in the operando NMR spectrum, suggesting vacancy rich phases, $Li_{13-\zeta}Sn_5$ and $Li_{7-\zeta}Sn_3$, with higher lithium mobility. Analysis of PDF measurements reveal that the metastable $Li_{7-\zeta}Sn_3$ phase has the structural framework of Li_7Sn_3 even as significant Li, $\zeta = 1.6$, is removed.

The capacity fade of ~30% per cycle is not attributed to particle cracking, but rather to particles losing contact with the carbon/PVDF binder. The disconnecting particles are associated with Li_xSn phases undergoing large decreases in diameters on delithiation, *i.e.*, Sn, Li_2Sn_5, LiSn, and Li_7Sn_3. A peculiar behavior of capacity fade in this system is that it only occurs during delithiation. An additional and related peculiar behavior is that the ^{7}Li resonances of the disconnected Li_xSn phases present at the end of each cycle disappear every time the cell is fully lithiated. These disconnected Li_xSn-containing particles remain in the electrode and become reconnected to the circuit by the volume increase of neighboring connected particles during the lithiation process. After multiple cycles the entire electrode material becomes converted primarily into disconnecting–reconnecting Li_xSn particles.

Although the capacity fade mechanism is simple, we are not aware of any *in situ* microscopy method capable of detecting and following such a disconnection–connection mechanism. Our approach clearly show the power of operando NMR spectroscopy for revealing such fundamental processes. We believe these results point the way for future efforts in both industrial and academic research labs to reduce capacity fade in a wider range of nano-structured intermetallic electrodes, involving Si, Ge and Sb, and suggests strategies such as functionalizing particle surfaces[54–56] and the use of more elastic binders.[57,58] Our disconnecting–reconnecting particles model of capacity fade also suggests exploring strategies for optimizing and implementing electrode nanoparticles packings that maintain electrical contact through multiple expansions and contractions.

Conflicts of interest

There are no conflicts to declare.

Acknowledgements

This research is supported in part by the USA National Science Foundation under Seed Grant NSF-DMR1420451. J. L. L. L. acknowledges the support of the GAANN fellowship from the Department of Education (P200A150267) and the Ohio State Department of Chemistry and Biochemistry. We thank Karena W. Chapman, Kamila M. Wiaderek, and Olaf J. Borkiewicz for helping with the PDF experiments. We also thank Vicky V. T. Doan-Nguyen for the discussions on PDF fitting. We acknowledge Brennan J. Walder for help with the initial NMR measurements, and Joshua T. Billy and Julen Bascaran for the SEM images. PDF measurements were performed at the Advanced Photon Source at Argonne National Laboratory.

Notes and references

1 A. N. Dey, *J. Electrochem. Soc.*, 1971, **118**, 1547.
2 M. Winter and J. O. Besenhard, *Electrochim. Acta*, 1999, **45**, 31–50.
3 D. Larcher, S. Beattie, M. Morcrette, K. Edstroem, J.-C. Jumas and J.-M. Tarascon, *J. Mater. Chem.*, 2007, **17**, 3759–3772.
4 C.-M. Park, J.-H. Kim, H. Kim and H.-J. Sohn, *Chem. Soc. Rev.*, 2010, **39**, 3115.
5 B. Wang, B. Luo, X. Li and L. Zhi, *Mater. Today*, 2012, **15**, 544–552.

6 I. A. Courtney and J. R. Dahn, *J. Electrochem. Soc.*, 1997, **144**, 2045.
7 C. J. Wen, *J. Electrochem. Soc.*, 1981, **128**, 1181.
8 W.-J. Zhang, *J. Power Sources*, 2011, **196**, 13–24.
9 C. J. Wen and R. A. Huggins, *J. Electrochem. Soc.*, 1981, **128**, 1181–1187.
10 J. Sangster and C. Bale, *J. Phase Equilib. Diffus.*, 1998, **19**, 70–75.
11 K. J. Rhodes, R. Meisner, M. Kirkham, N. Dudney and C. Daniel, *J. Electrochem. Soc.*, 2012, **159**, A294–A299.
12 J. Yang, M. Wachtler, M. Winter and J. O. Besenhard, *Electrochem. Solid-State Lett.*, 1999, **2**, 161.
13 L. Y. Beaulieu, K. C. Hewitt, R. L. Turner, A. Bonakdarpour, A. A. Abdo, L. Christensen, K. W. Eberman, L. J. Krause and J. R. Dahn, *J. Electrochem. Soc.*, 2003, **150**, A149.
14 T. D. Hatchard, J. M. Topple, M. D. Fleischauer and J. R. Dahn, *Electrochem. Solid-State Lett.*, 2003, **6**, A129.
15 A. D. W. Todd, P. P. Ferguson, M. D. Fleischauer and J. R. Dahn, *Int. J. Energy Res.*, 2010, **34**, 535–555.
16 M. Ebner, F. Marone, M. Stampanoni and V. Wood, *Science*, 2013, **342**, 716–720.
17 L. Y. Beaulieu, S. D. Beattie, T. D. Hatchard and J. R. Dahn, *J. Electrochem. Soc.*, 2003, **150**, A419.
18 L. Wang, Z. Xu, S. Yang, X. Tian, J. Wei, W. Wang and X. Bai, *Sci. China: Technol. Sci.*, 2013, **56**, 2630–2635.
19 A. S. Aricó, P. Bruce, B. Scrosati, J.-M. Tarascon and W. van Schalkwijk, *Nat. Mater.*, 2005, **4**, 366–377.
20 M. R. Wagner, P. R. Raimann, A. Trifonova, K.-C. Moeller, J. O. Besenhard and M. Winter, *Electrochem. Solid-State Lett.*, 2004, **7**, A201–A205.
21 A. Wang, S. Kadam, H. Li, S. Shi and Y. Qi, *npj Comput. Mater.*, 2018, **4**, 1–26.
22 H. Li, L. Shi, W. Lu, X. Huang and L. Chen, *J. Electrochem. Soc.*, 2001, **148**, A915–A922.
23 H. Li, X. Huang, L. Chen, Z. Wu and Y. Liang, *Electrochem. Solid-State Lett.*, 1999, **2**, 547–549.
24 R. E. Gerald, R. J. Klinger, G. Sandi, C. S. Johnson, L. G. Scanlon and J. W. Rathke, *J. Power Sources*, 2000, **89**, 237–243.
25 F. Chevallier, M. Letellier, M. Morcrette, J.-M. Tarascon, E. Frackowiak, J.-N. Rouzaud and F. Béguin, *Electrochem. Solid-State Lett.*, 2003, **6**, A225–A228.
26 B. Key, R. Bhattacharyya, M. Morcrette, V. Seznéc, J.-M. Tarascon and C. P. Grey, *J. Am. Chem. Soc.*, 2009, **131**, 9239–9249.
27 J. L. Lorie Lopez, P. J. Grandinetti and A. C. Co, *J. Mater. Chem. A*, 2018, **6**, 231–243.
28 J.-M. Tarascon, A. Gozdz, C. Schmutz, F. Shokoohi and P. Warren, *Solid State Ionics*, 1996, **86–88**, 49–54.
29 M. Letellier, F. Chevallier and M. Morcrette, *Carbon*, 2007, **45**, 1025–1034.
30 A. P. Hammersley, S. O. Svensson, M. Hanfland, A. N. Fitch and D. Hausermann, *High Pressure Res.*, 1996, **14**, 235–248.
31 X. Qiu, J. W. Thompson and S. J. L. Billinge, *J. Appl. Crystallogr.*, 2004, **37**, 678.
32 C. L. Farrow, P. Juhas, J. W. Liu, D. Bryndin, E. S. Božin, J. Bloch, T. Proffen and S. J. L. Billinge, *J. Phys.: Condens. Matter*, 2007, **19**, 335219.
33 A. J. Ilott, S. Chandrashekar, A. Klöckner, H. J. Chang, N. M. Trease, C. P. Grey, L. Greengard and A. Jerschow, *J. Magn. Reson.*, 2014, **245**, 143–149.
34 PhySy Ltd., RMN, 2018, http://www.physyapps.com.
35 J. L. Markley, W. J. Horsley and M. P. Klein, *J. Chem. Phys.*, 1971, **55**, 3604–3605.
36 E. Bekaert, F. Robert, P. Lippens and M. Ménétrier, *J. Phys. Chem. C*, 2010, **114**, 6749–6754.
37 A. J. Smith, J. C. Burns, X. Zhao, D. Xiong and J. R. Dahn, *J. Electrochem. Soc.*, 2011, **158**, A447.
38 M. A. McArthur, S. Trussler and J. R. Dahn, *J. Electrochem. Soc.*, 2012, **159**, A198–A207.
39 C. v. d. Marel, W. Geertsma and W. v. d. Lugt, *J. Phys. F: Met. Phys.*, 1980, **10**, 2305–2312.
40 K. Furuya, K. Ogawa, Y. Mineo, A. Matsufuji, J. Okuda and T. Erata, *J. Phys.: Condens. Matter*, 2001, **13**, 3519–3532.
41 C. van der Marel, A. B. van Oosten, W. Gertsma and W. van der Lugt, *J. Phys. F: Met. Phys.*, 1982, **12**, 2349–2361.
42 J. Wang, I. D. Raistrick and R. A. Huggins, *J. Electrochem. Soc.*, 1986, **133**, 457.
43 M. Mayo and A. J. Morris, *Chem. Mater.*, 2017, **29**, 5787–5795.
44 R. W. G. Wyckoff, *Crystal structures*, Krieger Publishing, Malabar, Fla, 1982, vol. 1.
45 D. A. Hansen and L. J. Chang, *Acta Crystallogr., Sect. B: Struct. Crystallogr. Cryst. Chem.*, 1978, **25**, 2392–2395.
46 W. Muller and H. Schafer, *Z. Naturforsch., B: Anorg. Chem., Org. Chem.*, 1973, **28**, 246–248.
47 W. Muller, *Z. Naturforsch., B: Anorg. Chem., Org. Chem.*, 1974, **29**, 304–307.
48 U. Frank, W. Müller and H. Shäfer, *Z. Naturforsch., B: Anorg. Chem., Org. Chem.*, 1975, **30**, 1–5.
49 U. Frank and W. Muller, *Z. Naturforsch., B: Anorg. Chem., Org. Chem.*, 1975, **30**, 316–322.
50 U. Frank, W. Muller and H. Schafer, *Z. Naturforsch., B: Anorg. Chem., Org. Chem.*, 1975, **30**, 6–9.
51 I. A. Courtney, J. S. Tse, O. Mao, J. Hafner and J. R. Dahn, *Phys. Rev. B: Condens. Matter Mater. Phys.*, 1998, **58**, 15583–15588.
52 K. M. Jensen, P. Juhas, M. A. Tofanelli, C. L. Heinecke, G. Vaughan, C. J. Ackerson and S. J. L. Billinge, *Nat. Commun.*, 2016, **7**, 11859.
53 X. H. Liu, L. Zhong, S. Huang, S. X. Mao, T. Zhu and J. Y. Huang, *ACS Nano*, 2012, **6**, 1522–1531.
54 S. Neudeck, F. Walther, T. Bergfeldt, C. Suchomski, M. Rohnke, P. Hartmann, J. Janek and T. Brezesinski, *ACS Appl. Mater. Interfaces*, 2018, **10**, 20487–20498.
55 P. K. Alaboina, M.-J. Uddin and S.-J. Cho, *Nanoscale*, 2017, **9**, 15736–15752.
56 S. Jiang, B. Hu, R. Sahore, L. Zhang, H. Liu, L. Zhang, W. Lu, B. Zhao and Z. Zhang, *ACS Appl. Mater. Interfaces*, 2018, **10**, 44924–44931.
57 T. Li, J.-y. Yang and S.-g. Lu, *Int. J. Miner., Metall. Mater.*, 2012, **19**, 752–756.
58 R. Wang, L. Feng, W. Yang, Y. Zhang, Y. Zhang, W. Bai, B. Liu, W. Zhang, Y. Chuan, Z. Zheng and H. Guan, *Nanoscale Res. Lett.*, 2017, **12**, 575.

Electronic Supplemental Information for *Phase Transformations and Capacity Fade Mechanism in Li_xSn Nanoparticle Electrodes Revealed by Operando ^7Li NMR*

Jose L. Lorie Lopez, Philip J. Grandinetti, Anne C. Co
Department of Chemistry and Biochemistry, The Ohio State University,
100 West 18th Ave. Columbus OH, 43210-1340, USA

Li Site	x	x_{Sn}	δ/ppm	T_1/s
Li_2Sn_5	0.4	0.7143	78	0.98 ± 0.05
LiSn	1.0	0.50	42	1.98 ± 0.04
LiSn	1.0	0.50	32	1.87 ± 0.01
Li_7Sn_3	$2.\overline{3}$	0.30	17.5	2.63 ± 0.30
Li_5Sn_2	2.5	0.286	14.3	2.63 ± 0.30
$Li_{13}Sn_5$	$2.\overline{6}$	0.278	16.7	2.63 ± 0.30
Li_7Sn_2	3.5	0.222	9.5	-
$Li_{7-\zeta}Sn_3$	1.8	0.30	$\sim$15	1.83 ± 0.03

Table S1: ^{7}Li magnetization longitudinal relaxation times and shifts determined in-situ in a Li-Sn cell during the lithiation/delithiation of the first cycle. All shift values of Li-Sn intermetallic phases were reported by Bekaert et al. [1] except for $Li_{7-\zeta}Sn_3$.

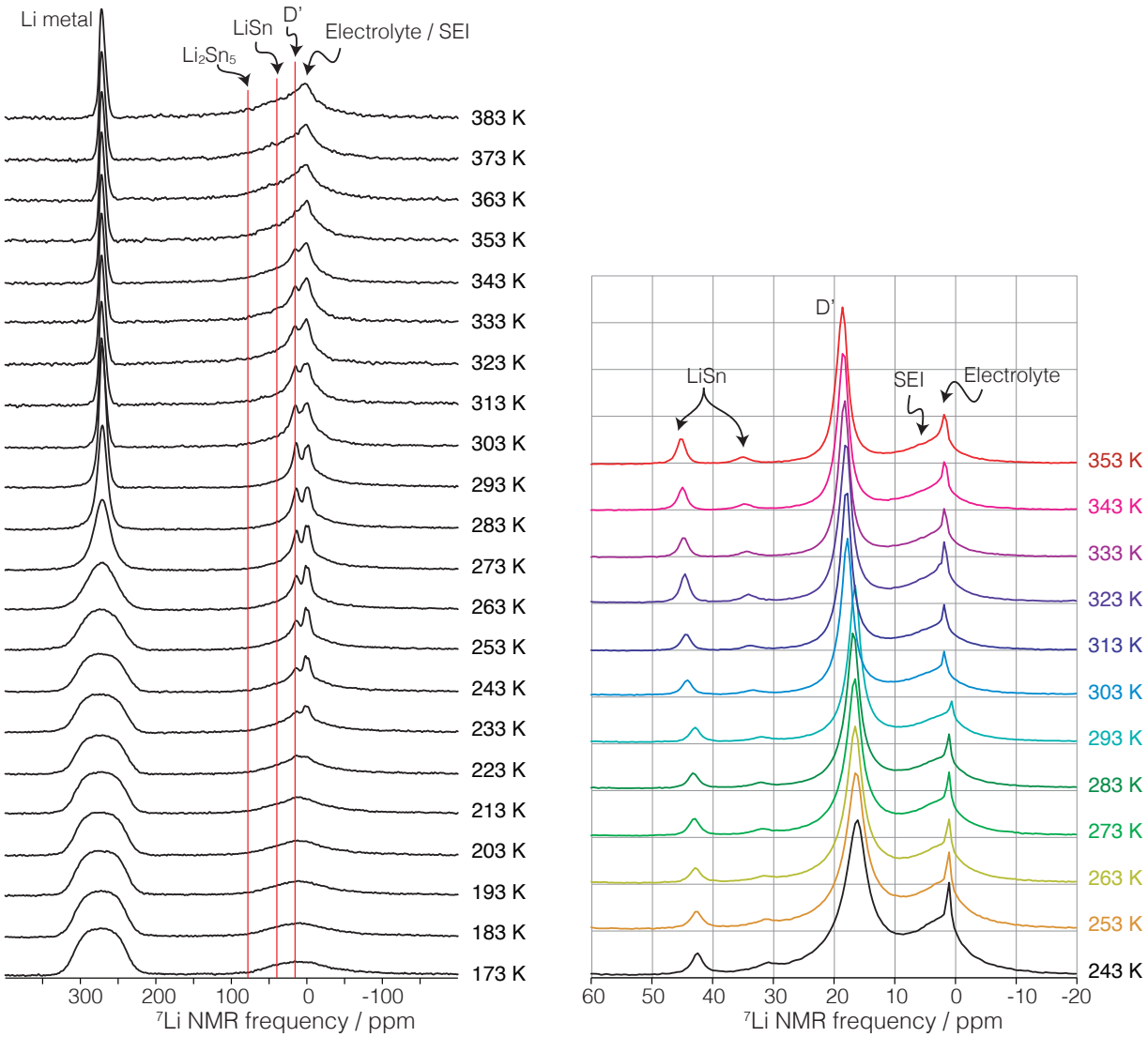

Figure S1: (A) In-situ variable temperature ^{7}Li static NMR spectra of a Sn electrode lithiated to $Li_{7-\zeta}Sn_3$. Spectra were obtained using an rf power of 150 W. A 5 μs pulse length was used giving a tip angle of 36 ° for the intermetallics and electrolyte, and 72 ° for the Li metal. A recycle delay of 0.65 s was used and 440 scans were averaged together for each spectrum. (B) Ex-situ variable temperature ^{7}Li MAS NMR spectra of the $Li_{7-\zeta}Sn_3$. Spectra were acquired with a Bruker 4 mm MAS probe at a spinning speed of 12 kHz and a $\pi/2$ pulse length of a 4 μs at 50 W, with 8 scans. A 45 s recycle delay was used for measurements between 243 K and 283K, a 30 s recycle delay for measurements between 293 K and 333K, and a 20 s delay for the measurements at 343 K and 353 K.

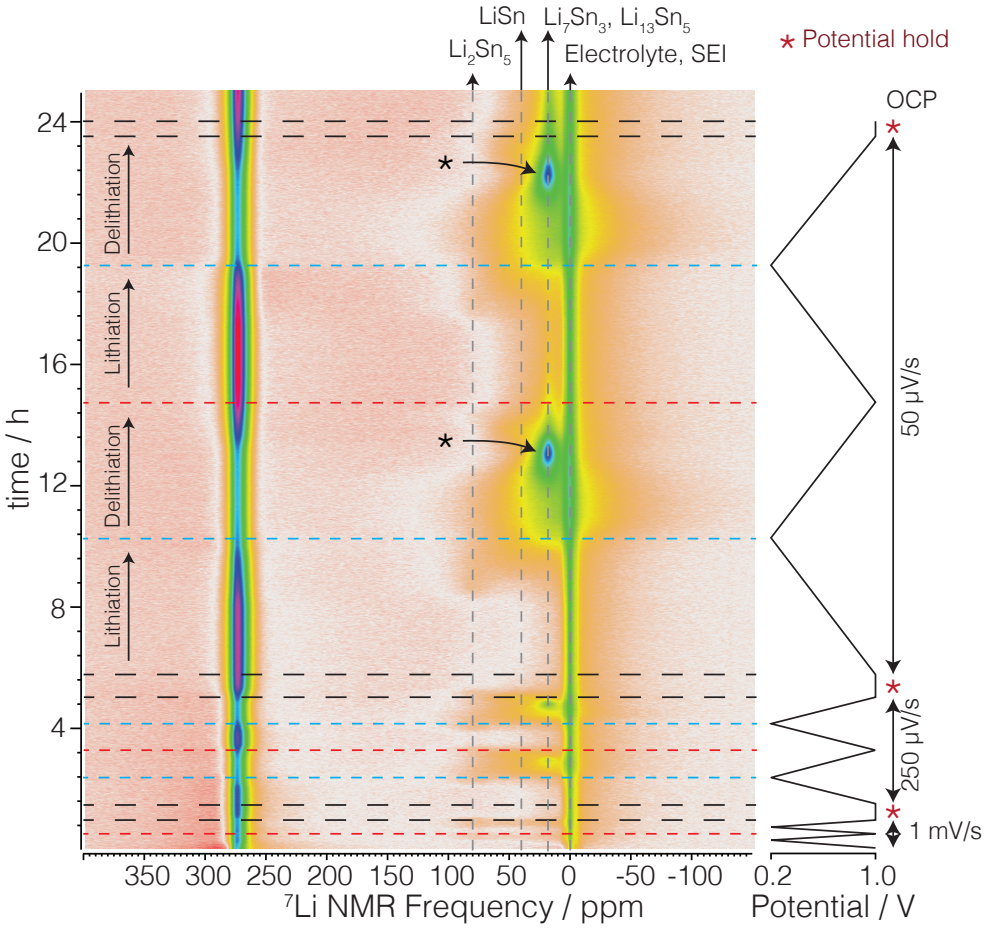

Figure S2: The effect of sweep rates on the lithiation and delithiation of Sn electrodes was examined with operando ^{7}Li NMR 2D spectra of a Sn electrode at 1000, 250, and 50 μV/s. Thirty minutes of potential hold at 1.0 V was conducted between each cycling regimes. During the first two cycles at 1000 μV/s only small signals of Li_2Sn_5 and LiSn are present even though the potential is swept to 0.2 V. This is consistent with previous observations that only the electrode surface is involved in the electrochemical Li process, particularly at relatively fast scan rates [2]. The next two cycles at 250 μV/s show characteristics of the formation of the Li_7Sn_3 group at 17.5 ppm and Li_7Sn_2 at 9.5 ppm. As the scan rate is decreased to 50 μV/s, the amount of lithiated Sn increases, where the formation of Li_7Sn_3 and Li_7Sn_2 is clearly present. During delithiation, the $Li_{7-\zeta}Sn_3$ phase also appears and becomes more intense during subsequent cycles.

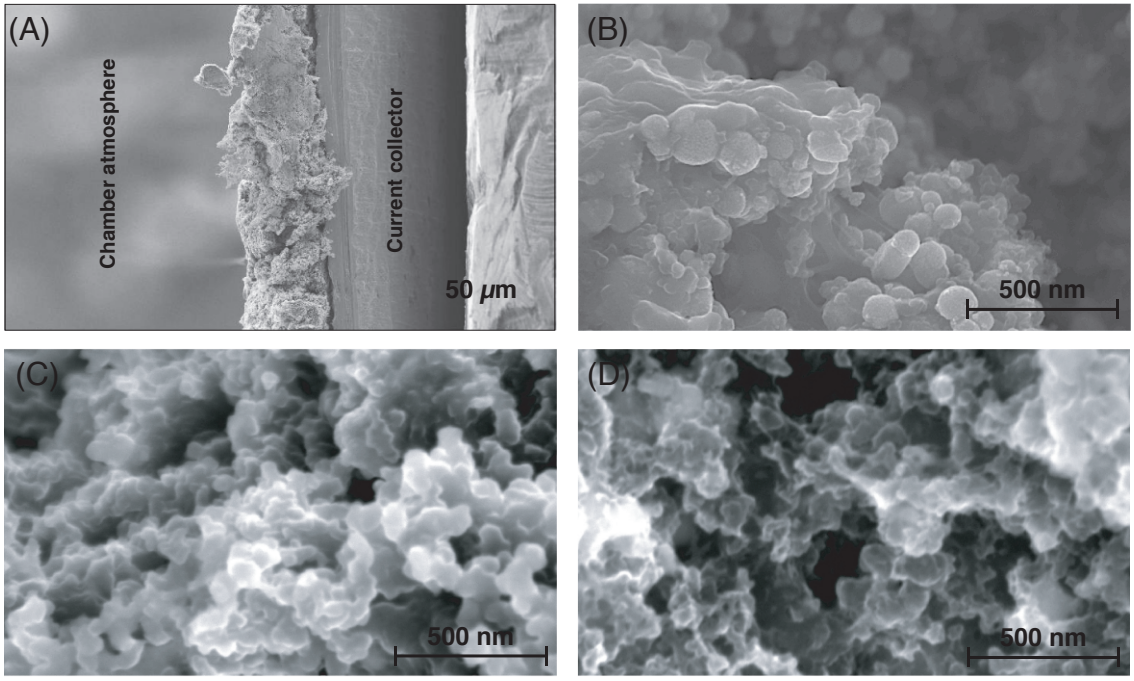

Figure S3: A FEI/Philips Sirion Field Emission scanning electron microscope (SEM) was used to probe the electrode surface morphology, as well as the uniformity of the electrode's thickness and the micrographs. In (A) is the SEM showing the thickness of the as-prepared electrode. In (B) is the SEM image of a fresh electrode, in (C) is the SEM image of the electrode cycled to Li_7Sn_3, and in (D) is the SEM image of the electrode cycled to the vacancy rich $Li_{7-\zeta}Sn_3$. When casted into an electrode film, the Sn nanoparticles maintained their 60-80 nm size, resulting in nanoporous features in the same order of magnitude. The Sn nanoparticle film is relatively uniform when casted giving an electrode thickness in the range of 30 - 40 μm. Once dried, the film contained macrochannels in the order of 150 - 200 μm.

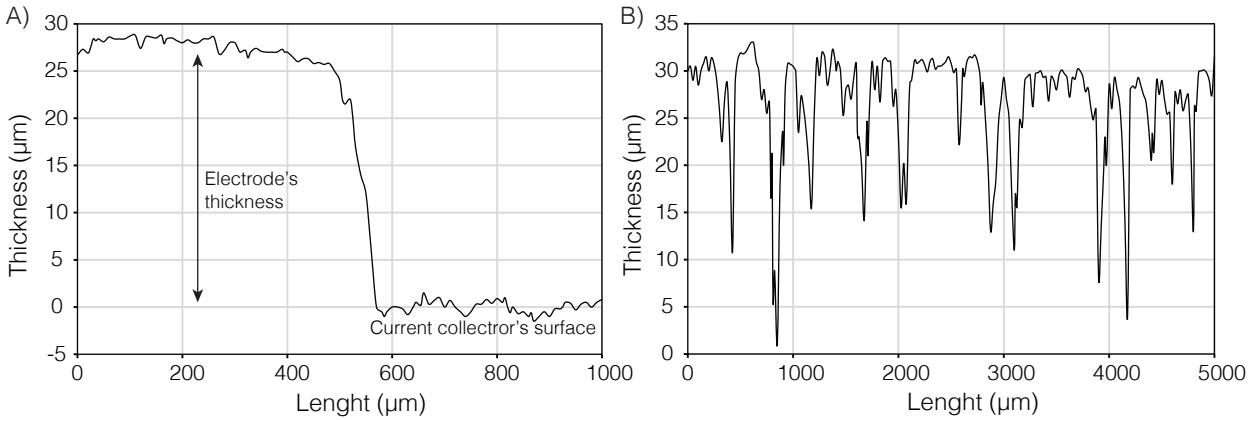

Figure S4: Surface profile of a fresh electrode showing in (A) that the electrode thickness measured as of ∼30 μm against the copper current collector surface and in (B) that the macroporous channels present in the electrode are between 150 to 250 μm wide. The electrode thickness was also measured using an Alpha-Step® 500 Surface Profiler with a stylus force of 25.9 mg and a scan rate of 50 μm/s.

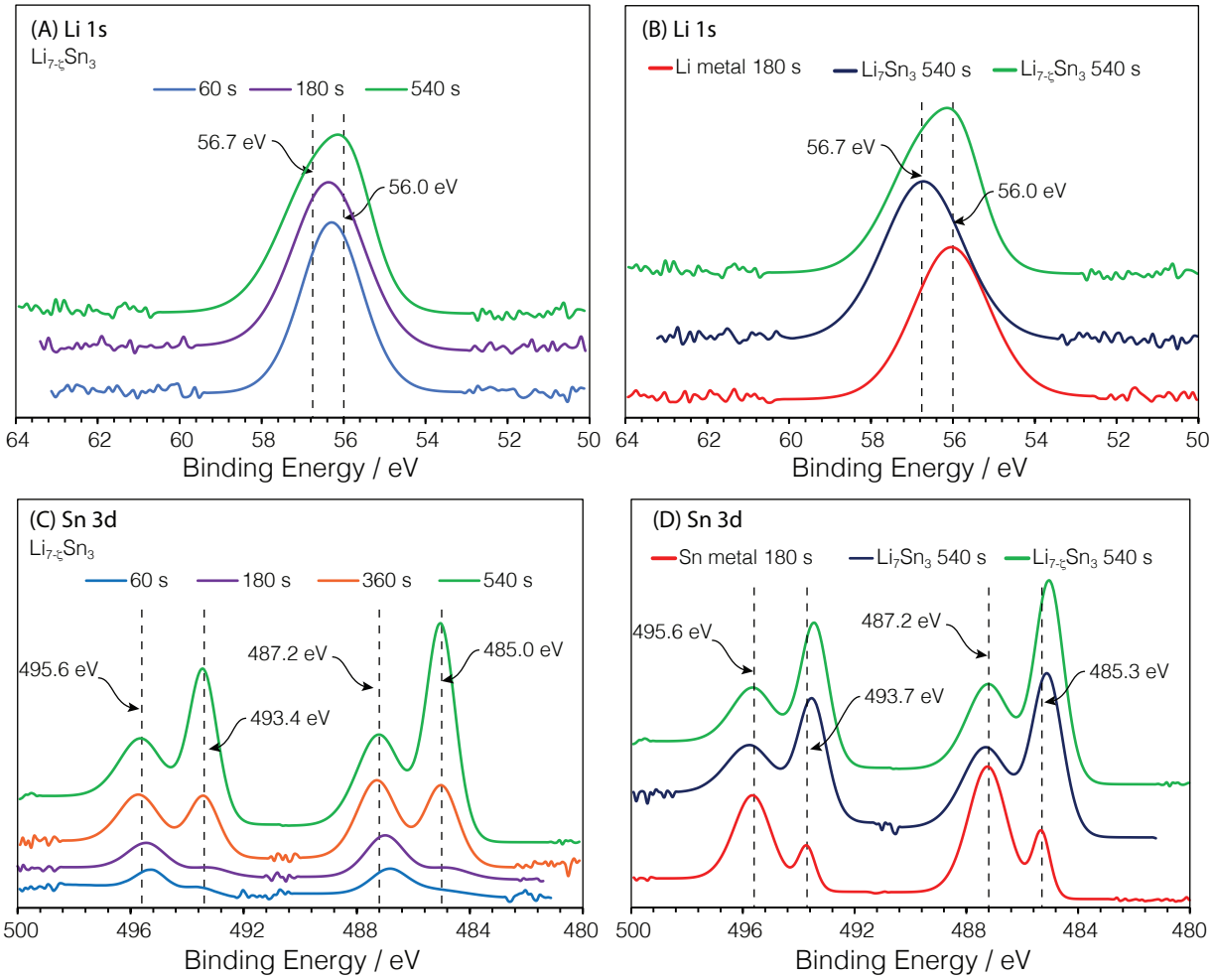

Figure S5: X-ray photoelectron microscopy was used to analyze any changes in the oxidation states of the lithium and tin in two samples, Li_7Sn_3 formed during lithiation, and the vacancy rich $Li_{7-\zeta}Sn_3$ formed during delithiation. In this figure are the X-ray photoelectron spectra of Li_7Sn_3 and $Li_{7-\zeta}Sn_3$ obtained during lithiation and delithiation, respectively. In (A) is the Li 1s spectra of the $Li_{7-\zeta}Sn_3$ as a function of etching time. In (B) is the Li 1s comparison of the $Li_{7-\zeta}Sn_3$ and Li_7Sn_3 to Li metal. In (C) is the Sn 3d spectra of the $Li_{7-\zeta}Sn_3$ as a function of etching time. In (D) is the Sn 3d comparison of the $Li_{7-\zeta}Sn_3$ and Li_7Sn_3 to Sn metal. The Li 1s shows a shift and peak broadening while the Sn 3d shows the emergence of the metallic Sn peaks at 485.0 and 493.4 eV for the Sn 3/2 and 5/2, respectively. The SnO_2 peaks at 487.2 and 495.6 eV, however, show minor changes in intensity as the electrode is composed of nanoparticles and their surface is always being probed. Comparing the peaks of the $Li_{7-\zeta}Sn_3$ to those of the reference metal and Li_7Sn_3, the Li 1s in (B) reveals a shift of 0.7 eV for Li_7Sn_3 with respect to the lithium metal. The $Li_{7-\zeta}Sn_3$ on the other hand, exhibits a broad peak with contributions from both the Li metal and the standard Li_7Sn_3. The Sn 3d result indicates that the Sn 3/2 peak at 485.3 eV for both Li_7Sn_3 and $Li_{7-\zeta}Sn_3$ are shifted 0.3 eV from that of metallic Sn, indicating that the oxidation states of Li and Sn in Li_7Sn_3 and $Li_{7-\zeta}Sn_3$ are very similar and that their structures are related.

References

[1] Emilie Bekaert, F. Robert, P.E. Lippens, and M.Ménétrier. ^{7}Li NMR Knight shifts in Li-Sn compounds: MAS NMR measurements and correlation with DFT calculations. *J. Phys. Chem. C*, 114:6749–6754, 2010.

[2] D. X. Liu, J. Wang, K. Pan, J. Qiu, M. Canova, L. R. Cao, and A. C. Co. In situ quantification and visualization of lithium transport with neutrons. *Angew. Chem. Int. Edit.*, 53:9498 – 9502, 2014.